PHYSICAL REVIEW C **97**, 054304 (2018)

Microscopically based energy density functionals for nuclei using the density matrix expansion. II. Full optimization and validation

R. Navarro Pérez,[1,*] N. Schunck,[2,†] A. Dyhdalo,[3,‡] R. J. Furnstahl,[3,§] and S. K. Bogner[4,‖]

[1] *Institute of Nuclear and Particle Physics and Department of Physics and Astronomy, Ohio University, Athens, Ohio 45701, USA*
[2] *Nuclear and Chemical Sciences Division, Lawrence Livermore National Laboratory, Livermore, California 94551, USA*
[3] *Department of Physics, The Ohio State University, Columbus, Ohio 43210, USA*
[4] *National Superconducting Cyclotron Laboratory and Department of Physics and Astronomy,*
Michigan State University, East Lansing, Michigan 48824, USA

(Received 25 January 2018; published 2 May 2018)

Background: Energy density functional methods provide a generic framework to compute properties of atomic nuclei starting from models of nuclear potentials and the rules of quantum mechanics. Until now, the overwhelming majority of functionals have been constructed either from empirical nuclear potentials such as the Skyrme or Gogny forces, or from systematic gradient-like expansions in the spirit of the density functional theory for atoms.
Purpose: We seek to obtain a usable form of the nuclear energy density functional that is rooted in the modern theory of nuclear forces. We thus consider a functional obtained from the density matrix expansion of local nuclear potentials from chiral effective field theory. We propose a parametrization of this functional carefully calibrated and validated on selected ground-state properties that is suitable for large-scale calculations of nuclear properties.
Methods: Our energy functional comprises two main components. The first component is a non-local functional of the density and corresponds to the direct part (Hartree term) of the expectation value of local chiral potentials on a Slater determinant. Contributions to the mean field and the energy of this term are computed by expanding the spatial, finite-range components of the chiral potential onto Gaussian functions. The second component is a local functional of the density and is obtained by applying the density matrix expansion to the exchange part (Fock term) of the expectation value of the local chiral potential. We apply the UNEDF2 optimization protocol to determine the coupling constants of this energy functional.
Results: We obtain a set of microscopically constrained functionals for local chiral potentials from leading order up to next-to-next-to-leading order with and without three-body forces and contributions from Δ excitations. These functionals are validated on the calculation of nuclear and neutron matter, nuclear mass tables, single-particle shell structure in closed-shell nuclei, and the fission barrier of ^{240}Pu. Quantitatively, they perform noticeably better than the more phenomenological Skyrme functionals.
Conclusions: The inclusion of higher-order terms in the chiral perturbation expansion seems to produce a systematic improvement in predicting nuclear binding energies while the impact on other observables is not really significant. This result is especially promising since all the fits have been performed at the single-reference level of the energy density functional approach, where important collective correlations such as center-of-mass correction, rotational correction, or zero-point vibrational energies have not been taken into account yet.

DOI: 10.1103/PhysRevC.97.054304

I. INTRODUCTION

Chiral effective field theory (χ_{EFT}) provides the framework for the modern theory of nuclear forces [1,2]. It allows the systematic construction of nuclear interaction potentials from first principles by introducing an expansion of the momentum and pion mass over the chiral symmetry breaking scale (of the order of 1 GeV). Using chiral interactions to compute properties of heavy nuclei relevant to applications such as fission, nucleosynthesis, or superheavy science poses a number of challenges. These interactions are presumed to represent realistic in-medium nuclear forces. Therefore, they should only be used in the framework of many-body methods that fully incorporate all many-body correlations induced by these potentials. In light nuclei, the no-core shell model [3] or quantum Monte Carlo methods [4] are popular examples of such direct approaches; in heavier nuclei, alternative methods such as the coupled-cluster [5] or in-medium similarity renormalization group [6] can provide good approximations of the exact many-body solution for nuclei near closed shells. In spite of very impressive recent success, the majority of nuclei remain out of reach of *ab initio* methods, and the most microscopic approach available relies on the nuclear energy density functional (EDF) formalism [7].

---

[*] navarrop@ohio.edu
[†] schunk1@llnl.gov
[‡] dyhdalo.2@osu.edu
[§] furnstahl.1@osu.edu
[‖] bogner@nscl.msu.edu

The EDF approach stands in contrast to *ab initio* approaches in that it is based on enforcing that the wave function of the nucleus takes a simple form such as a Slater determinant in the Hartree-Fock (HF) theory or a quasiparticle vacuum in the Hartree-Fock-Bogoliubov (HFB) theory.[1] By definition, such an ansatz for the many-body wave function cannot be compatible with the use of realistic potentials, and most energy functionals are instead derived from phenomenological nucleon-nucleon (NN) potentials such as the zero-range Skyrme potential or the finite-range Gogny force [7,8]. The parameters of these effective NN forces are typically adjusted on properties of nuclear matter or finite nuclei. These phenomenological EDFs do not rely on a systematic, perturbative expansion. As a consequence, there is no mathematical proof that generalizing these EDFs with, e.g., terms up to higher orders in relative momenta (see Refs. [9–11]) or finite-range gradient terms [12] will yield a better predictive power. A similar statement can be made about EDFs directly built out of various powers of the local density and its gradient such as the BPCM [13–15] or SEALL1 [16] functionals: while providing great flexibility and physics insight, the exact predictive power of these functionals is difficult to assess.

For these reasons, one would like to combine the predictive power, systematic power-counting scheme, and connection to quantum chromodynamics (QCD) of chiral potentials with the computational scaling, versatility, and physics intuition of phenomenological potentials. One route to achieving this is based on the density matrix expansion (DME) of expectation values [17–20]. Thanks to the Wick theorem, the expectation value of an arbitrary potential on a product state can be expressed as a functional of the one-body density matrix (or generalized density if pairing correlations are present). In the general case, the density matrix is fully non-local, that is, of the form $\rho(\boldsymbol{r}\sigma\tau,\boldsymbol{r}'\sigma'\tau')$ with σ and τ the spin and isospin projections, respectively. The basic idea of the DME is to expand ρ around the local density $\rho(\boldsymbol{r})$ in order to turn the expectation value of the potential into a functional of the local density and gradient-like corrections.

The method was first outlined by Negele and Vautherin [17,18]. Several refinements to the original method to increase its accuracy were proposed in Refs. [19–22]. In Ref. [23], the DME was applied to both the direct and exchange terms of the HF expectation value for unregulated momentum-space chiral potentials. The parameters of the resulting EDF were adjusted approximately using the singular value decomposition algorithm, and were tested in calculations of radii, single-particle spectra in doubly closed shell nuclei, and deformation energy. While promising, the authors reported numerical instabilities in the practical implementation of the DME and emphasized that direct terms were treated in the local density approximation and that tensor contributions to the EDF had been neglected.

The goal of this paper is to remedy some of these limitations, in particular by taking into account recent developments in χ_{EFT} and employing high performance computing tools. Precisely, we want to fully calibrate and validate an energy functional constrained by *local* chiral nuclear potentials. To this end, we build the EDF (in the particle-hole (p-h) channel) by computing the expectation value of chiral potentials on a Slater determinant. We use the DME of local chiral potentials presented in Ref. [24] to recast the exchange contribution in the form of a local functional of the density. We adjust the coupling constants of this EDF to ground-state properties of finite nuclei by solving the HFB equation. We provide results for EDFs corresponding to different orders in the chiral expansion up to next-to-next-to-leading (N2LO) order. Δ excitations and three-nucleon ($3N$) forces are included.

The paper is organized as follows. In Sec. II, we recall the expressions for NN and $3N$ chiral potentials in coordinate space. Section III describes how these potentials can be transformed into an EDF with the DME (more details are given in Ref. [24]) and how these EDFs are implemented in current density functional theory (DFT) solvers. We also provide in that section the result of our calibration process. In Sec. IV, we test the predictive power of these EDFs on the equation of state of nuclear matter, mass tables, single-particle (s.p.) energies of doubly closed shell nuclei, and the fission barrier of ^{240}Pu. Finally, we present some conclusions and perspectives in Sec. V.

II. LOCAL CHIRAL POTENTIAL IN COORDINATE SPACE

We consider local chiral potentials up to N2LO with and without Δ excitations including also $3N$ forces [25,26]. Chiral interactions contain finite- and zero-range contributions, with the zero-range couplings usually fine-tuned to reproduce low-energy πN and NN scattering data along with selected few-body properties and sometimes properties of nuclei up to oxygen [25–30]. In the present work, we implement the finite-range contributions "as is," since they correspond to the long-range pion physics, which is well described by χ_{EFT}. In contrast, the zero-range contribution is replaced by a Skyrme-like potential, and we take the contact coupling constants as adjustable parameters to be determined on selected properties of finite nuclei.

The finite-range contributions depend on a few sets of parameters including the pion mass m_π, the $\Delta - N$ mass splitting $M_{\Delta-N}$, the pion decay constant f_π, the nucleon axial vector coupling g_A, the N-to-Δ axial vector coupling h_A, as well as the low-energy coupling constants (LECs) c_1, c_2, c_3, and c_4 and the LECs linear combination $b_3 + b_8$[2]. Although the values for most of these parameters are well determined, the LECs have been determined through different analyses of low-energy πN and NN scattering observables yielding different results [32–39]. For this particular work, we use the determination of Ref. [37] and leave the study of the impact of the value of the LECs for a future work.

Since the finite-range potentials obtained from their corresponding diagrams diverge as r goes to zero, in practice a

---

[1] This statement applies in the single-reference energy density functional (SR-EDF) version of the EDF approach. In its multireference energy density functional (MR-EDF) version, one needs to consider two different reference states.

[2] For simplicity we retain the $b_3 + b_8$ combination even though it has been shown to be redundant [31].

short-range regulator is used to make scattering and structure calculations feasible. While several arguments have been made about the effects of the regulator on the statistical and systematic uncertainties [25,40,41], for this work we restrict ourselves to the particular regulator

$$f(r) = \left[1 - \exp\left(-\frac{r^2}{R_c^2}\right)\right]^n, \tag{1}$$

with $R_c = 1.0$ fm and $n = 6$. We also leave the study of the dependence on the strength of the regulator controlled by the R_c and n parameters for a future work. The inclusion of the regulator is one of the improvements over the early work of [23]. In the two following sections we recall the expressions for the long-range part only of the NN and $3N$ chiral potentials.

A. Two-body potential

The finite-range contribution to the local chiral potential in coordinate space is given by

$$\begin{aligned} V_\chi(\boldsymbol{r}) = {} & (V_C(r) + W_C(r)\boldsymbol{\tau}_1\cdot\boldsymbol{\tau}_2) \\ & + (V_S(r) + W_S(r)\boldsymbol{\tau}_1\cdot\boldsymbol{\tau}_2)\boldsymbol{\sigma}_1\cdot\boldsymbol{\sigma}_2 \\ & + (V_T(r) + W_T(r)\boldsymbol{\tau}_1\cdot\boldsymbol{\tau}_2)\hat{S}_{12}(\hat{\boldsymbol{r}}), \end{aligned} \tag{2}$$

where $r \equiv |\boldsymbol{r}|$, $\hat{S}_{12}(\hat{\boldsymbol{r}})$ is the usual tensor operator

$$\hat{S}_{12}(\hat{\boldsymbol{r}}) = 3(\boldsymbol{\sigma}_1\cdot\hat{\boldsymbol{r}})(\boldsymbol{\sigma}_2\cdot\hat{\boldsymbol{r}}) - \boldsymbol{\sigma}_1\cdot\boldsymbol{\sigma}_2, \tag{3}$$

and $\boldsymbol{\sigma}_i$ ($\boldsymbol{\tau}_i$) is the spin (isospin) operator for the ith particle. The potential components at leading order (LO) correspond to the well-known one-pion exchange and are given by

$$W_S^{\mathrm{LO}}(r) = \frac{m_\pi^3}{12\pi}\left(\frac{g_A}{2f_\pi}\right)^2 Y(r), \tag{4}$$

$$W_T^{\mathrm{LO}}(r) = \frac{m_\pi^3}{12\pi}\left(\frac{g_A}{2f_\pi}\right)^2 Y(r)T(r), \tag{5}$$

where $Y(r)$, $U(r)$, and $T(r)$ are the usual Yukawa, scalar, and tensor functions, respectively,

$$Y(r) = \frac{e^{-x}}{x}, \quad U(r) = 1 + \frac{1}{x}, \quad T(r) = 1 + \frac{3}{x}U(r), \tag{6}$$

with $x = m_\pi r$. The potential components at next-to-leading order (NLO) including only nucleons and pions are given by

$$\begin{aligned} W_C^{\mathrm{NLO}}(r) = {} & +\frac{m_\pi^5}{8\pi^3(2f_\pi)^4}\frac{1}{x^4} \\ & \times \left\{x\left[1 + 10g_A^2 - g_A^4(23 + 4x^2)\right]K_0(2x)\right. \\ & \left. + \left[1 + 2g_A^2(5 + 2x^2) - g_A^4(23 + 12x^2)\right]K_1(2x)\right\}, \end{aligned} \tag{7}$$

$$\begin{aligned} V_S^{\mathrm{NLO}}(r) = {} & +\frac{m_\pi^5}{2\pi^3}\left(\frac{g_A}{2f\pi}\right)^4 \\ & \times \frac{1}{x^4}\left[3xK_0(2x) + (3 + 2x^2)K_1(2x)\right], \end{aligned} \tag{8}$$

$$\begin{aligned} V_T^{\mathrm{NLO}}(r) = {} & -\frac{m_\pi^5}{8\pi^3}\left(\frac{g_A}{2f\pi}\right)^4 \\ & \times \frac{1}{x^4}\left[12xK_0(2x) + (15 + 4x^2)K_1(2x)\right], \end{aligned} \tag{9}$$

where $K_0(x)$ and $K_1(x)$ are the modified Bessel functions of the second kind. The potential components at N2LO including only nucleons and pions are given by

$$\begin{aligned} V_C^{\mathrm{N2LO}}(r) = {} & +\frac{3}{2}\frac{g_A^2 m_\pi^6}{(2f_\pi)^4\pi^2}\frac{e^{-2x}}{x^6}\left[2c_1x^2(1 + x)^2\right. \\ & \left. + c_3(6 + 12x + 10x^2 + 4x^3 + x^4)\right], \end{aligned} \tag{10}$$

$$W_S^{\mathrm{N2LO}}(r) = +\frac{1}{3}\frac{g_A^2 m_\pi^6}{(2f_\pi)^4\pi^2}\frac{e^{-2x}}{x^6}c_4(1 + x)(3 + 3x + 2x^2), \tag{11}$$

$$W_T^{\mathrm{N2LO}}(r) = -\frac{1}{3}\frac{g_A^2 m_\pi^6}{(2f_\pi)^4\pi^2}\frac{e^{-2x}}{x^6}c_4(1 + x)(3 + 3x + x^2). \tag{12}$$

The expressions for the potential components coming from one- and two-Δ excitations can be found in the supplemental material of Ref. [24].

B. Three-body potential

A general, local, three-body potential consists of all permutations with respect to the three two-body subsystems,

$$V^{3N} = V_{12} + V_{23} + V_{13}, \tag{13}$$

where the V_{ij} potential depends on two of the relative coordinates and the spin and isospin of the three particles,

$$V_{ij} = V(\boldsymbol{r}_{ik}, \boldsymbol{r}_{jk}, \sigma_1, \tau_1, \sigma_2, \tau_2, \sigma_3, \tau_3), \quad \boldsymbol{r}_{ij} = \boldsymbol{r}_i - \boldsymbol{r}_j. \tag{14}$$

Because of the symmetry of the potential under subscript interchange in the DME implementation (see Ref. [24]) only one of the three terms in Eq. (13) is necessary to express the full three-body potential. For definiteness, we choose $V_{23}(\boldsymbol{r}_{21}, \boldsymbol{r}_{31}, \{\sigma\tau\})$.

The different terms appearing in the $3N$ chiral potential can be classified as (i) long range, which are vertices of c_i or h_A and have no Dirac δ functions, (ii) intermediate range, which are vertices of c_i, h_A, or c_D and have one Dirac δ function, and (iii) short range, which are vertices of c_i, h_A, c_D, or c_E with two Dirac δ functions. In our implementation of the $3N$ chiral interaction in an EDF, we include only the long-range terms along with the c_i and h_A intermediate-range terms. We assume that all short-range terms and c_D vertices can be effectively absorbed by the optimization of the contact couplings on nuclear properties.

There is no contribution from $3N$ potentials up to N2LO, unless Δ excitations are included. The $3N$ potentials at NLO with Δ and N2LO have a very similar structure that can be summarized as

$$V_{3N}^{\mathrm{NLO}\Delta} = \sum_{i=1}^{3}\alpha_i^{\mathrm{NLO}\Delta}V_{C,i}, \tag{15}$$

$$V_{3N}^{\mathrm{N2LO}} = \sum_{i=1}^{3}\alpha_i^{\mathrm{N2LO}}V_{C,i} + V_D + V_E. \tag{16}$$

We employ the NLOΔ label to emphasize that this contribution is only present when the Δ contributions are included. As mentioned before, the V_D (short-range term controlled by c_D)

and V_E (short-range term controlled by c_E) terms are in fact not included in the present implementation. The α_i prefactors are given by

$$\alpha_1^{\mathrm{NLO}\Delta} = 0, \quad \alpha_2^{\mathrm{NLO}\Delta} = -\frac{h_A^2 m_\pi^6 g_A^2}{2592 f_\pi^4 \pi^2 M_{\Delta-N}},$$
$$\alpha_3^{\mathrm{NLO}\Delta} = \frac{h_A^2 m_\pi^6 g_A^2}{10368 f_\pi^4 \pi^2 M_{\Delta-N}}, \tag{17}$$

and

$$\alpha_1^{\mathrm{N2LO}} = \frac{c_1 m_\pi^6 g_A^2}{16 f_\pi^4 \pi^2}, \quad \alpha_2^{\mathrm{N2LO}} = \frac{c_3 m_\pi^6 g_A^2}{288 f_\pi^4 \pi^2},$$
$$\alpha_3^{\mathrm{N2LO}} = \frac{c_4 m_\pi^6 g_A^2}{576 f_\pi^4 \pi^2}, \tag{18}$$

and the $V_{C,i}$ potentials are given by

$$V_{C,1} = (\boldsymbol{\tau}_2 \cdot \boldsymbol{\tau}_3)(\boldsymbol{\sigma}_2 \cdot \hat{\boldsymbol{r}}_{21})(\boldsymbol{\sigma}_3 \cdot \hat{\boldsymbol{r}}_{31}) U(r_{21}) Y(r_{21}) U(r_{31}) Y(r_{31}), \tag{19}$$

$$\begin{aligned} V_{C,2} = (\boldsymbol{\tau}_2 \cdot \boldsymbol{\tau}_3)\Bigg\{ & \frac{16\pi^2}{m_\pi^6}(\boldsymbol{\sigma}_2 \cdot \boldsymbol{\sigma}_3)\delta^3(\boldsymbol{r}_{21})\delta^3(\boldsymbol{r}_{31}) - \frac{4\pi}{m_\pi^3}\big[S_{23}(\hat{\boldsymbol{r}}_{21})T(r_{21}) + (\boldsymbol{\sigma}_2 \cdot \boldsymbol{\sigma}_3)\big] Y(r_{21})\delta^3(\boldsymbol{r}_{31}) \\ & - \frac{4\pi}{m_\pi^3}\big[S_{23}(\hat{\boldsymbol{r}}_{31})T(r_{31}) + (\boldsymbol{\sigma}_2 \cdot \boldsymbol{\sigma}_3)\big] Y(r_{31})\delta^3(\boldsymbol{r}_{21}) \\ & + \big[9(\boldsymbol{\sigma}_2 \cdot \hat{\boldsymbol{r}}_{21})(\boldsymbol{\sigma}_3 \cdot \hat{\boldsymbol{r}}_{31})(\hat{\boldsymbol{r}}_{21} \cdot \hat{\boldsymbol{r}}_{31}) - 3(\boldsymbol{\sigma}_2 \cdot \hat{\boldsymbol{r}}_{21})(\boldsymbol{\sigma}_3 \cdot \hat{\boldsymbol{r}}_{21}) - 3(\boldsymbol{\sigma}_2 \cdot \hat{\boldsymbol{r}}_{31})(\boldsymbol{\sigma}_3 \cdot \hat{\boldsymbol{r}}_{31}) + (\boldsymbol{\sigma}_2 \cdot \boldsymbol{\sigma}_3)\big] T(r_{21})Y(r_{21})T(r_{31})Y(r_{31}) \\ & + (\boldsymbol{\sigma}_2 \cdot \boldsymbol{\sigma}_3) Y(r_{21})Y(r_{31}) + S_{23}(\hat{\boldsymbol{r}}_{21})T(r_{21})Y(r_{21})Y(r_{31}), + S_{23}(\hat{\boldsymbol{r}}_{31})T(r_{31})Y(r_{31})Y(r_{21}) \Bigg\}, \end{aligned} \tag{20}$$

$$\begin{aligned} V_{C,3} = \boldsymbol{\tau}_2 \cdot (\boldsymbol{\tau}_3 \times \boldsymbol{\tau}_1)\Bigg\{ & \frac{16\pi^2}{m_\pi^6}\delta^3(\boldsymbol{r}_{21})\delta^3(\boldsymbol{r}_{31})\boldsymbol{\sigma}_2 \cdot (\boldsymbol{\sigma}_3 \times \boldsymbol{\sigma}_1) \\ & - \frac{12\pi}{m_\pi^3}(\boldsymbol{\sigma}_2 \cdot \hat{\boldsymbol{r}}_{21})\hat{\boldsymbol{r}}_{21} \cdot (\boldsymbol{\sigma}_3 \times \boldsymbol{\sigma}_1)T(r_{21})Y(r_{21})\delta^3(\boldsymbol{r}_{31}) + \frac{4\pi}{m_\pi^3}\boldsymbol{\sigma}_2 \cdot (\boldsymbol{\sigma}_3 \times \boldsymbol{\sigma}_1)\frac{3}{m_\pi r_{21}}U(r_{21})Y(r_{21})\delta^3(\boldsymbol{r}_{31}) \\ & - \frac{12\pi}{m_\pi^3}(\boldsymbol{\sigma}_3 \cdot \hat{\boldsymbol{r}}_{31})\hat{\boldsymbol{r}}_{31} \cdot (\boldsymbol{\sigma}_1 \times \boldsymbol{\sigma}_2)T(r_{31})Y(r_{31})\delta^3(\boldsymbol{r}_{21}) + \frac{4\pi}{m_\pi^3}\boldsymbol{\sigma}_2 \cdot (\boldsymbol{\sigma}_3 \times \boldsymbol{\sigma}_1)\frac{3}{m_\pi r_{31}}U(r_{31})Y(r_{31})\delta^3(\boldsymbol{r}_{21}) \\ & + 9(\boldsymbol{\sigma}_2 \cdot \hat{\boldsymbol{r}}_{21})(\boldsymbol{\sigma}_3 \cdot \hat{\boldsymbol{r}}_{31})\boldsymbol{\sigma}_1 \cdot (\hat{\boldsymbol{r}}_{21} \times \hat{\boldsymbol{r}}_{31})T(r_{21})Y(r_{21})T(r_{31})Y(r_{31}) \\ & - 3(\boldsymbol{\sigma}_2 \cdot \hat{\boldsymbol{r}}_{21})\hat{\boldsymbol{r}}_{21} \cdot (\boldsymbol{\sigma}_3 \times \boldsymbol{\sigma}_1)T(r_{21})\frac{3}{m_\pi r_{31}}U(r_{31})Y(r_{21})Y(r_{31}) \\ & - 3(\boldsymbol{\sigma}_3 \cdot \hat{\boldsymbol{r}}_{31})\hat{\boldsymbol{r}}_{31} \cdot (\boldsymbol{\sigma}_1 \times \boldsymbol{\sigma}_2)T(r_{31})\frac{3}{m_\pi r_{21}}U(r_{21})Y(r_{21})Y(r_{31}) \\ & - \boldsymbol{\sigma}_1 \cdot (\boldsymbol{\sigma}_2 \times \boldsymbol{\sigma}_3)\frac{3}{m_\pi r_{21}}U(r_{21})\frac{3}{m_\pi r_{31}}U(r_{31})Y(r_{21})Y(r_{31}) \Bigg\}, \end{aligned} \tag{21}$$

where the Yukawa $Y(r)$, scalar $U(r)$, and tensor $T(r)$ functions are defined in Eqs. (6). As mentioned above, short-range terms with two Dirac δ functions are not included in the DME implementation of the $3N$ interaction as we expect their effect to be absorbed by the calibration of the EDF contact couplings.

III. IMPLEMENTATION OF χEFT IN DFT

In our implementation of chiral interactions in the DFT framework, we seek to write the total energy of a nucleus in the following form:

$$E = E_\chi^{\mathrm{Har}} + E_\chi^{\mathrm{Skyrme}} + E^{\mathrm{Coul}} + E^{\mathrm{pair}}. \tag{22}$$

The first term is the Hartree (direct) contribution to the expectation value of the long-range part of the local chiral potentials on Slater-determinant reference states. In practice, we see below that only the two-body chiral potential contributes to it because we only work with time-even systems. The second term is formally identical to an extended Skyrme-like functional and contains the effects of *both* the short-range part of the chiral potentials (in an effective way) and the exchange contribution from the long-range part (through the DME). Finally, the terms E^{Coul} and E^{pair} are the usual Coulomb and pairing energies, obtained here by following exactly the same recipes as in Refs. [42–44].

Two remarks are in order at this point:

(i) It should be clear from Eq. (22) that we restrict ourselves to the SR-EDF level. In other words, we seek to calibrate a functional built out of a single HFB reference state in complete analogy with, e.g., the UNEDF family of functionals [42–44], the BPCM functional [13–15], or the SEALL functional [16,45]. As a result, we expect our functional to be limited in its description of the fine structure of $N = Z$ nuclei, for instance mirror displacement energies where isospin mixing and restoration are essential [46] or the arc-like structure of binding energies near closed-shell nuclei caused by quadrupole correlation energies [47,48]. We should also expect limitations in describing the shell structure of closed-shell nuclei, where effects such as particle-vibration couplings should be taken into account [49].

(ii) In this work, we take pairing functionals derived from a zero-range, surface-volume, two-body force as in the UNEDF functionals. The primary motivation for this choice is to focus on the effect of the DME on the p-h channel only before considering its application to the p-p channel. Early studies of pairing observables in finite nuclei with chiral potentials also suggest that it is mostly the short-range part of the latter that affects the p-p channel [50–52]. Finally, since we work at the SR-EDF level, the consistency of the generating kernels between the two channels is not really an issue.

To achieve the decomposition (22), we express the expectation value of chiral potentials on a Slater determinant reference state. In Sec. III A, we briefly recall how this works for the two-body channel (2): the Hartree term is expanded as a sum of Gaussians, while the Fock term is transformed into a generalized Skyrme functional with the DME. In Sec. III B, we give the expressions for the three-body channel, where only the Fock term contributes; detailed derivations can be found in Ref. [24].

A. Two-body potentials

In configuration space, the contribution to the energy from a two-body potential reads

$$E^{NN} = \frac{1}{2}\sum_{ij}\langle ij|\mathcal{V}_{\chi}^{NN}|kl\rangle\rho_{ki}\rho_{lj}, \tag{23}$$

with ρ_{ij} the matrix elements of the one-body density matrix on an arbitrary basis of the single-particle Hilbert space. The two-body potential is antisymmetrized,

$$\mathcal{V}_{\chi}^{NN} = V_{\chi}^{NN}(1 - P_{\sigma}P_{\tau}P_{r}), \tag{24}$$

with the usual spin-, isospin-, and space-exchange operators P_σ, P_τ, and P_r:

$$P_{\sigma} \equiv \tfrac{1}{2}(1 + \boldsymbol{\sigma}_1\cdot\boldsymbol{\sigma}_2), \quad P_{\tau} \equiv \tfrac{1}{2}(1 + \boldsymbol{\tau}_1\cdot\boldsymbol{\tau}_2). \tag{25}$$

The antisymmetrization operator results in direct and exchange contributions, also referred to as the Hartree and Fock energies, respectively.

After transforming Eq. (23) to coordinate space by inserting resolutions of the identity, changing to relative ($\boldsymbol{r}$) and center-of-mass ($\boldsymbol{R}$) coordinates and assuming translational invariance along with a local potential, the two-body interaction energy term becomes

$$\begin{aligned}E^{NN} = {}& \frac{1}{2}\mathrm{Tr}_1\mathrm{Tr}_2\int d\boldsymbol{R}\int d\boldsymbol{r}\ \langle \boldsymbol{r}\sigma_1\tau_1\sigma_2\tau_2|V_{\chi}(\boldsymbol{r})|\boldsymbol{r}\sigma_3\tau_3\sigma_4\tau_4\rangle\\ &\times\left[\rho_1\left(\boldsymbol{R}+\frac{\boldsymbol{r}}{2}\right)\rho_2\left(\boldsymbol{R}-\frac{\boldsymbol{r}}{2}\right)\right.\\ &\left.-\rho_1\left(\boldsymbol{R}-\frac{\boldsymbol{r}}{2},\boldsymbol{R}+\frac{\boldsymbol{r}}{2}\right)\rho_2\left(\boldsymbol{R}+\frac{\boldsymbol{r}}{2},\boldsymbol{R}-\frac{\boldsymbol{r}}{2}\right)P_{12}^{\sigma\tau}\right],\end{aligned} \tag{26}$$

where the traces refer to summation over spin and isospin quantum numbers and the local density matrix is

$$\rho(\boldsymbol{x}) \equiv \rho(\boldsymbol{x},\boldsymbol{x}). \tag{27}$$

The first term in Eq. (26) corresponds to the Hartree energy, while the second one corresponds to the Fock energy. The following sections describe our implementation of each of these two terms.

1. Hartree term

The one-body density matrix in Eq. (26) can be decomposed into scalar-isoscalar, scalar-isovector, vector-isoscalar, and vector-isovector components [7]:

$$\begin{aligned}\rho(\boldsymbol{x}\sigma_1\tau_1,\boldsymbol{y}\sigma_2\tau_2) = {}& \tfrac{1}{4}[\rho_0(\boldsymbol{x},\boldsymbol{y}) + \rho_1(\boldsymbol{x},\boldsymbol{y})\tau_z\\ &+ \boldsymbol{S}_0(\boldsymbol{x},\boldsymbol{y})\cdot\boldsymbol{\sigma} + \boldsymbol{S}_1(\boldsymbol{x},\boldsymbol{y})\cdot\boldsymbol{\sigma}\tau_z].\end{aligned} \tag{28}$$

Inserting this decomposition into the first term of Eq. (26) and performing the traces, one obtains

$$\begin{aligned}E_{\mathrm{H}} = {}& \frac{1}{2}\sum_{t=0,1}\int d\boldsymbol{r}\int d\boldsymbol{R}\ \big[\rho_t(\boldsymbol{R}^{+})\rho_t(\boldsymbol{R}^{-})\Gamma_{\rho\rho}^{t}\\ &+ \boldsymbol{S}_t(\boldsymbol{R}^{+})\cdot\boldsymbol{S}_t(\boldsymbol{R}^{-})\Gamma_{SS}^{t}\\ &+ (\boldsymbol{S}_t(\boldsymbol{R}^{+})\cdot\hat{\boldsymbol{r}})(\boldsymbol{S}_t(\boldsymbol{R}^{-})\cdot\hat{\boldsymbol{r}})\Gamma_{Sr}^{t}\big],\end{aligned}$$

where $\boldsymbol{R}^{\pm} = \boldsymbol{R} \pm \frac{\boldsymbol{r}}{2}$ and

$$\Gamma_{\rho\rho}^{t} = \begin{cases} V_C & \text{for} \quad t = 0\\ W_C & \text{for} \quad t = 1,\end{cases} \tag{29a}$$

$$\Gamma_{SS}^{t} = \begin{cases} V_S - V_T & \text{for} \quad t = 0\\ W_S - W_T & \text{for} \quad t = 1,\end{cases} \tag{29b}$$

$$\Gamma_{Sr}^{t} = \begin{cases} 3\ V_T & \text{for} \quad t = 0\\ 3\ W_T & \text{for} \quad t = 1,\end{cases} \tag{29c}$$

with $t = 0$ ($t = 1$) indicating the isoscalar (isovector) case. Note that for systems with time-reversal symmetry, all terms diagonal in the spin density vanish; i.e., $\boldsymbol{S}(\boldsymbol{x}) = 0$. Hence, for even-even nuclei, only the terms proportional to the central part of the potential in $\Gamma_{\rho\rho}^{t}$ contribute to the Hartree energy.

At this stage the DME could be applied to the calculation of the Hartree energy. However, it has been established that computing this term exactly provides a more precise description of the density fluctuations and energy contribution [18,53]. Furthermore, the inclusion of the DME approximation in the calculation of the Hartree field introduces numerical instabilities [23]. For these reasons, we choose to compute the direct term exactly. To compute the matrix element of the finite range of the chiral potential, we expand the Yukawa form factors on a series of Gaussian functions [54]. This allows us to take full advantage of the many analytic properties of Gaussian matrix elements in the harmonic oscillator basis [55] and of the existing implementation of the Gogny force in the latest version of HFBTHO [56]. As we show in Fig. 1, five Gaussian functions already give an excellent approximation to the spatial part of the potential.

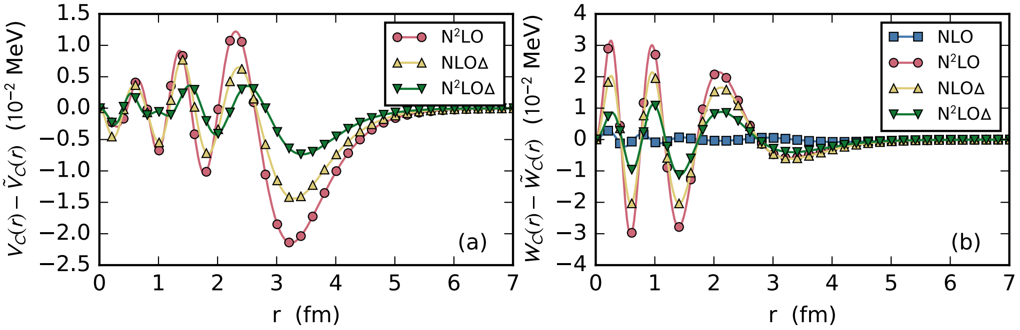

FIG. 1. Difference between the potentials $V_C(\boldsymbol{r})$ and $W_C(\boldsymbol{r})$ up to a certain chiral order and their corresponding approximations by a sum of five Gaussian functions shown in Eqs. (32) and (33).

The chiral potential in Eq. (2) is expressed in a spin-isospin operator basis. In the code HFBTHO [56], the finite-range part of the Gogny functional is implemented in an exchange operator basis; that is,

$$V_{\mathrm{G}} = \sum_{i=1}^{N}(W_i + B_i P_\sigma + H_i P_\sigma P_\tau + M_i P_\sigma P_\tau)e^{-\boldsymbol{r}^2/\mu_i^2}. \quad (30)$$

After inserting the definitions of Eq. (25) and rewriting the terms in the Gogny functional, we find

$$V_{\mathrm{G}} = \sum_{i=1}^{N}\bigg[W_i + \frac{B_i}{2} + \frac{H_i}{2} + \frac{M_i}{4} + \left(\frac{B_i}{2} + \frac{M_i}{4}\right)\boldsymbol{\sigma}_1\cdot\boldsymbol{\sigma}_2 + \left(\frac{H_i}{2} + \frac{M_i}{4}\right)\boldsymbol{\tau}_1\cdot\boldsymbol{\tau}_2 + \frac{M_i}{4}(\boldsymbol{\sigma}_1\cdot\boldsymbol{\sigma}_2)(\boldsymbol{\tau}_1\cdot\boldsymbol{\tau}_2)\bigg]e^{-r^2/\mu_i^2}. \quad (31)$$

Since only systems with time-reversal symmetry are being considered for this work, only the central components of the chiral potential are considered in Eq. (2). Therefore, we can set $B_i = M_i = 0$ and use the approximations

$$V_C(\boldsymbol{r}) \to \tilde{V}_C(\boldsymbol{r}) = \sum_{i=1}^{N}\left(W_i + \frac{H_i}{2}\right)e^{-\boldsymbol{r}^2/\mu_i^2}, \quad (32)$$

$$W_C(\boldsymbol{r}) \to \tilde{W}_C(\boldsymbol{r}) = \sum_{i=1}^{N}\frac{H_i}{2}e^{-\boldsymbol{r}^2/\mu_i^2}. \quad (33)$$

In order to reproduce the behavior of the regulator in Eq. (1) the conditions

$$H_N = -\sum_{i=1}^{N-1}H_i, \quad W_N = -\sum_{i=1}^{N-1}W_i, \quad (34)$$

are imposed. These conditions ensure that the potentials vanish as $r \to 0$. The remaining free parameters W_i, H_i, and μ_i are adjusted numerically to reproduce the central components of the chiral potential at different orders. In Fig. 1 we show the difference between the approximations as a sum of five Gaussian functions and the corresponding chiral potential up to a certain order in the chiral expansion. Note that while the scale in Fig. 1 is 1×10^{-2} MeV the potentials have an order of magnitude, at their highest values, of 10 MeV.

2. Fock term

Inserting Eq. (28) into the second term of Eq. (26), the two-body Fock term becomes

$$E_{\mathrm{F}} = -\frac{1}{2}\sum_{t=0,1}\int d\boldsymbol{r}\int d\boldsymbol{R}\big[\rho_t^2(\boldsymbol{R}^+,\boldsymbol{R}^-)\Xi^t_{\rho\rho} - \boldsymbol{S}_t^2(\boldsymbol{R}^+,\boldsymbol{R}^-)\Xi^t_{SS} - (\boldsymbol{S}_t(\boldsymbol{R}^+,\boldsymbol{R}^-)\cdot\hat{\boldsymbol{r}})^2\,\Xi^t_{Sr}\big], \quad (35)$$

where the symmetries $\rho_t(\boldsymbol{x},\boldsymbol{y}) = \rho_t(\boldsymbol{y},\boldsymbol{x})$ and $\boldsymbol{S}_t(\boldsymbol{x},\boldsymbol{y}) = -\boldsymbol{S}_t(\boldsymbol{y},\boldsymbol{x})$ for time-reversal-invariant systems are used and the Ξ^t functions are given by

$$\Xi^t_{\rho\rho} = \begin{cases}\frac{1}{4}V_C + \frac{3}{4}W_C + \frac{3}{4}V_S + \frac{9}{4}W_S & \text{for } t = 0\\ \frac{1}{4}V_C - \frac{1}{4}W_C + \frac{3}{4}V_S - \frac{3}{4}W_S & \text{for } t = 1,\end{cases} \quad (36a)$$

$$\Xi^t_{SS} = \begin{cases}\frac{1}{4}V_C + \frac{3}{4}W_C - \frac{1}{4}V_S - \frac{3}{4}W_S & \\ \qquad -\frac{1}{2}V_T - \frac{3}{2}W_T & \text{for } t = 0\\ \frac{1}{4}V_C - \frac{1}{4}W_C - \frac{1}{4}V_S + \frac{1}{4}W_S & \\ \qquad -\frac{1}{2}V_T + \frac{1}{2}W_T & \text{for } t = 1,\end{cases} \quad (36b)$$

$$\Xi^t_{Sr} = \begin{cases}\frac{3}{2}V_T + \frac{9}{2}W_T & \text{for } t = 0\\ \frac{3}{2}V_T - \frac{3}{2}W_T & \text{for } t = 1.\end{cases} \quad (36c)$$

The DME consists in expanding the non-diagonal density matrices in such manner that the non-locality is factorized using the following formula:

$$\rho_t(\boldsymbol{R}^+,\boldsymbol{R}^-) \approx \sum_{n=0}^{n_{\max}}\Pi_n^\rho(kr)\mathcal{P}_n(\boldsymbol{R}), \quad (37)$$

$$\boldsymbol{S}_t(\boldsymbol{R}^+,\boldsymbol{R}^-) \approx \sum_{m=0}^{m_{\max}}\Pi_m^s(kr)\mathcal{Q}_m(\boldsymbol{R}), \quad (38)$$

where the Π functions are specified by the DME variant, and $\mathcal{P}_n(\boldsymbol{R})$ and $\mathcal{Q}_m(\boldsymbol{R})$ denote various local densities. The arbitrary momentum scale k in the Π functions sets the scale for the fall-off in the off-diagonal direction. In this work, we follow common practice and truncate the expansion at $n_{\max} = 2$ and

$m_{\max} = 1$ such that

$$\rho_t(\boldsymbol{R}^+,\boldsymbol{R}^-) \approx \Pi_0^\rho(k_{\mathrm{F}}r)\rho_t(\boldsymbol{R}) + \frac{r^2}{6}\Pi_2^\rho\left[\frac{1}{4}\Delta\rho_t(\boldsymbol{R}) - \tau_t(\boldsymbol{R}) + \frac{3}{5}k_{\mathrm{F}}^2\rho_t(\boldsymbol{R})\right], \tag{39}$$

$$S_{t,b}(\boldsymbol{R}^+,\boldsymbol{R}^-) \approx i\,\Pi_1^s(k_{\mathrm{F}}r)\sum_{a=x}^{z} r_a J_{t,ab}(\boldsymbol{R}), \tag{40}$$

where the kinetic density τ_t and spin current density $\boldsymbol{J}_t$ are defined as

$$\tau_t(\boldsymbol{r}) = \nabla\cdot\nabla'\rho_t(\boldsymbol{r},\boldsymbol{r}')|_{\boldsymbol{r}=\boldsymbol{r}'}, \tag{41}$$

$$J_{t,ab}(\boldsymbol{r}) = -\frac{i}{2}(\nabla_a - \nabla'_a)S_{t,b}(\boldsymbol{r},\boldsymbol{r}')|_{\boldsymbol{r}=\boldsymbol{r}'}. \tag{42}$$

In Gebremariam's improved phase-space-averaging DME variant [19,20], the momentum scale k is chosen to be the Fermi momentum k_{F} with the Π functions given by

$$\Pi_0^\rho(k_{\mathrm{F}}r) = \Pi_2^\rho(k_{\mathrm{F}}r) = \Pi_1^s(k_{\mathrm{F}}r) = 3\frac{j_1(k_{\mathrm{F}}r)}{k_{\mathrm{F}}r}, \tag{43}$$

where j_1 is a spherical Bessel function of the first kind and k_{F} is related to the isoscalar density in the usual way:

$$k_{\mathrm{F}} = \left(\frac{3\pi^2}{2}\rho_0(\boldsymbol{R})\right)^{1/3}. \tag{44}$$

By inserting the expansions of Eqs. (39) and (40) into the exact Fock energy of Eq. (35), the Fock energy can be approximated by expressions involving only products of local densities. Terms beyond second order in the density expansions are dropped, e.g., $\Pi_2^\rho(k_{\mathrm{F}}r)\Pi_2^\rho(k_{\mathrm{F}}r)$. After performing the DME and organizing the different terms in Eq. (35) by the different densities, we find the more compact expression

$$E_{\mathrm{F}} \approx \sum_{t=0,1}\int d\boldsymbol{R}\,\big[g_t^{\rho\rho}\rho_t\rho_t + g_t^{\rho\tau}\rho_t\tau_t + g_t^{\rho\Delta\rho}\rho_t\Delta\rho_t + g_t^{JJ,1}J_{t,aa}J_{t,bb} + g_t^{JJ,2}J_{t,ab}J_{t,ab} + g_t^{JJ,3}J_{t,ab}J_{t,ba}\big], \tag{45}$$

where the $\boldsymbol{R}$ dependence of the local densities and couplings g is omitted for simplicity and the coupling functions are given by

$$g_t^{\rho\rho}(\rho_0) = -\frac{4\pi}{2}\int drr^2\left[\Pi_0^\rho(k_{\mathrm{F}}r)^2 + \frac{r^2k_{\mathrm{F}}^2}{5}\Pi_0^\rho(k_{\mathrm{F}}r)\Pi_2^\rho(k_{\mathrm{F}}r)\right]\Xi_{\rho\rho}^t(r), \tag{46a}$$

$$g_t^{\rho\tau}(\rho_0) = \frac{4\pi}{2}\int drr^2\left[\frac{r^2}{3}\Pi_0^\rho(k_{\mathrm{F}}r)\Pi_2^\rho(k_{\mathrm{F}})\right]\Xi_{\rho\rho}^t(r), \tag{46b}$$

$$g_t^{\rho\Delta\rho}(\rho_0) = -\frac{4\pi}{2}\int drr^2\left[\frac{r^2}{12}\Pi_0^\rho(k_{\mathrm{F}}r)\Pi_2^\rho(k_{\mathrm{F}})\right]\Xi_{\rho\rho}^t(r), \tag{46c}$$

$$g_t^{JJ,1}(\rho_0) = -\frac{4\pi}{2}\int drr^2\left[\frac{r^2}{15}\Pi_1^S(k_{\mathrm{F}}r)^2\right]\Xi_{Sr}^t(r), \tag{46d}$$

$$g_t^{JJ,2}(\rho_0) = -\frac{4\pi}{2}\int drr^2\left[\frac{r^2}{15}\Pi_1^S(k_{\mathrm{F}}r)^2\right]\left[5\,\Xi_{SS}^t(r) + \Xi_{Sr}^t(r)\right], \tag{46e}$$

$$g_t^{JJ,3}(\rho_0) = -\frac{4\pi}{2}\int drr^2\left[\frac{r^2}{15}\Pi_1^S(k_{\mathrm{F}}r)^2\right]\Xi_{Sr}^t(r). \tag{46f}$$

As already highlighted in Ref. [23], one of the practical differences between Skyrme and DME-based functionals is that each Skyrme coupling constant becomes a coupling function, which is dependent on the isoscalar density. The calculation of these density-dependent couplings requires performing several multidimensional numerical integrals, some of them converging slowly at small values of ρ_0. However, these couplings are completely independent of the system being calculated or any other characteristic of the HFB simulation like the basis size or oscillator length. Therefore, we can tabulate all the relevant coupling functions for different values of the density ρ_0. In the actual HFB calculation the couplings are approximated via the interpolating function

$$\tilde{g}^{uv}(\rho) = g^{uv}(0) + \sum_{i=1}^{N} a_i\tan^{-1}\left(b_i\rho_0^{c_i}\right). \tag{47}$$

The parameters of the interpolating functions were adjusted to reproduce the tabulated values using $N = 3$. While other forms of interpolating functions were considered, this one gave a better description of the coupling functions while avoiding numerically unstable behavior at small and large values of ρ_0. An additional advantage of using interpolating functions is that the inclusion of Δ excitations and $3N$ forces does not imply any increase on computational cost since the same type of interpolating function is used for all cases. Figure 2 shows the numerical precision of these interpolating functions for two-body couplings. While the numerical precision of the interpolation is of the order of 1×10^{-3} MeV fm^{-3}, this is four orders of magnitude smaller than the scale of the couplings themselves, which is of the order of 10 MeV fm^{-3}.

B. Three-body term

The contribution of the V_χ^{3N} three-body chiral potential to the total energy is given by

$$E^{3N} = \frac{1}{6}\sum_{ijk}\langle ijk|V_\chi^{3N}\mathcal{A}_{123}|lmn\rangle\rho_{li}\rho_{mj}\rho_{nk}, \tag{48}$$

with $\mathcal{A}_{123} = (1 + P_{13}P_{12} + P_{23}P_{12})(1 - P_{12})$ the full three-body antisymmetrization operator. Since all the terms in the $3N$ Hartree energy contain at least one spin density matrix, which vanishes in time-reversal-invariant systems, there is in fact no contribution from the $3N$ channel to the Hartree energy. The application of the DME to the Fock term results in 23 trilinears of local densities, each one with its corresponding density-dependent coupling:

$$E_{\mathrm{F}}^{3\mathrm{N}} \approx \int d\boldsymbol{R}\big(g^{\rho_0^3}\rho_0^3 + g^{\rho_0^2\tau_0}\rho_0^2\tau_0 + g^{\rho_0^2\Delta\rho_0}\rho_0^2\Delta\rho_0 + g^{\rho_0(\nabla\rho_0)^2}\rho_0\nabla\rho_0\cdot\nabla\rho_0 + g^{\rho_0\rho_1^2}\rho_0\rho_1^2 + g^{\rho_1^2\tau_0}\rho_1^2\tau_0 + g^{\rho_1^2\Delta\rho_0}\rho_1^2\Delta\rho_0 + g^{\rho_0\rho_1\tau_1}\rho_0\rho_1\tau_1 + g^{\rho_0\rho_1\Delta\rho_1}\rho_0\rho_1\Delta\rho_1$$

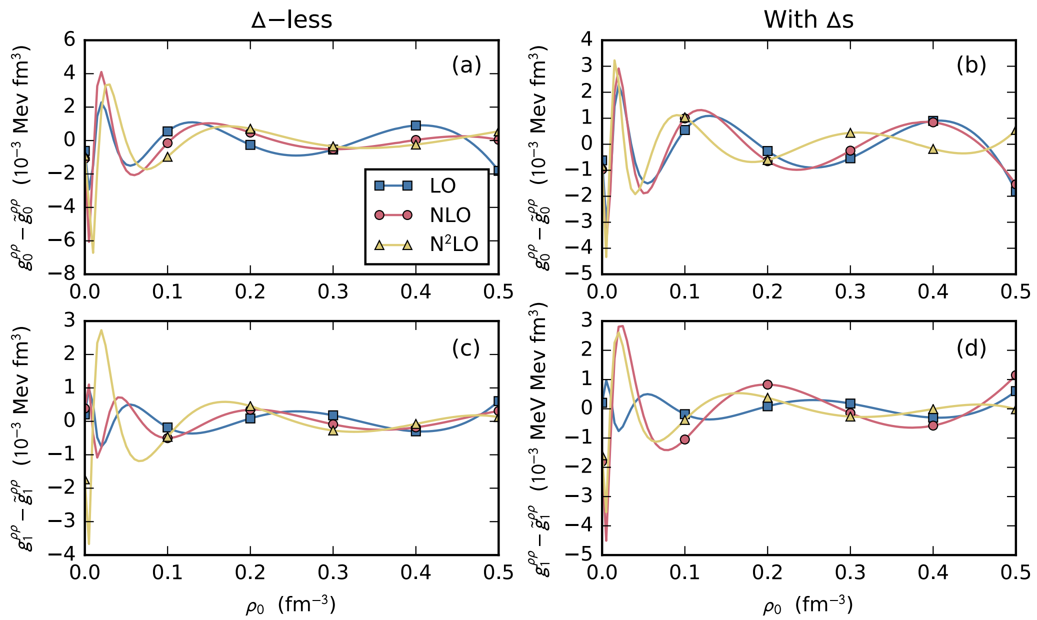

FIG. 2. Difference between the two-body density dependent couplings $g_t^{\rho\rho}$ and their corresponding interpolating function $\tilde{g}_t^{\rho\rho}$ given by Eq. (47).

$$\begin{aligned}&+g^{\rho_0(\nabla\rho_1)^2}\rho_0\nabla\rho_1\cdot\nabla\rho_1+\rho_0\epsilon_{ijk}[g^{\rho_0\nabla\rho_0J_0}\nabla_i\rho_0J_{0,jk}\\&+g^{\rho_0\nabla\rho_1J_1}\nabla_i\rho_1J_{1,jk}]+\rho_1\epsilon_{ijk}[g^{\rho_1\nabla\rho_1J_0}\nabla_i\rho_1J_{0,jk}\\&+g^{\rho_1\nabla\rho_0J_1}\nabla_i\rho_0J_{1,jk}]+\rho_0[g^{\rho_0J_0^2,1}J_{0,aa}J_{0,bb}\\&+g^{\rho_0J_0^2,2}J_{0,ab}J_{0,ab}+g^{\rho_0J_0^2,3}J_{0,ab}J_{0,ba}]\\&+\rho_0[g^{\rho_0J_1^2,1}J_{1,aa}J_{1,bb}+g^{\rho_0J_1^2,2}J_{1,ab}J_{1,ab}\\&+g^{\rho_0J_1^2,3}J_{1,ab}J_{1,ba}]+\rho_1[g^{\rho_0J_0J_1,1}J_{1,aa}J_{0,bb}\\&+g^{\rho_0J_0J_1,2}J_{1,ab}J_{0,ab}+g^{\rho_0J_0J_1,3}J_{1,ab}J_{0,ba}]).\end{aligned}\tag{49}$$

We refer the reader to Ref. [24] and its supplemental material for an in-depth derivation of the $3N$ energy Fock term and complete expressions for the density-dependent couplings. Similarly to the two-body case, the calculation of the density functions in terms of the density ρ_0 requires several multidimensional numerical integrals with slow convergence. To avoid calculating these coupling functions at every iteration of the HFB calculation, we employ the same type of interpolating function as in Eq. (47) and adjust its parameters to reproduce tabulated couplings. Figure 3 shows the accuracy of these interpolations at different chiral orders for two representative functions, $g^{\rho_0^3}$ and $g^{\rho_0\rho_1^2}$. The accuracy of the interpolation is comparable for all coupling functions. The irregularities in the curves show that the interpolation has an accuracy similar to the numerical multidimensional integral. As with two-body couplings, the numerical error of the interpolation is about four orders of magnitude smaller than the couplings themselves.

C. Optimization of contact couplings

Unlike *ab initio* methods in which many-body correlations are encoded into the nucleon wave functions, DFT assumes independent (quasi)particles through uncorrelated, product wave functions. Therefore, many-body correlations have to be included both through the form and parameters of the EDF (single- or multireference) and through the symmetry-breaking mechanism. Recall that in our decomposition (22) of the total energy, the Skyrme-like part is the sum of three terms: an effective two-body Skyrme functional that mocks up the effects of the short-range part of the chiral potentials, a generalized Skyrme functional of the form (45) that contains the exchange contribution of the two-body chiral potential, and a generalized Skyrme functional of the form (49) for the exchange contribution of the $3N$ channel. The two-body part thus reads

$$\begin{aligned}E_{NN}^{\text{Skyrme}}=\sum_{t=0,1}\int d\boldsymbol{R}\big[\big(U_{t0}^{\rho\rho}+U_{tD}^{\rho\rho}\rho_0^{\gamma}\big)\rho_t^2+U_t^{\rho\tau}\rho_t\tau_t\\+U_t^{\rho\Delta\rho}\rho_t\Delta\rho_t+U_t^{\rho\nabla J}\rho_t\nabla\cdot\boldsymbol{J}_t+U_t^{JJ}J_{t,ab}J_{t,ab}\big],\end{aligned}\tag{50}$$

where each coupling function is given by

$$U_t^{uu'}(\rho)=C_t^{uu'}+g_t^{uu'}[\rho_0(\boldsymbol{R})]\tag{51}$$

with the functions $g_t^{uu'}[\rho_0(\boldsymbol{R})]$ listed in Eqs. (46a)–(46f). The pairing energy is given by

$$E^{\text{pair}}=\frac{1}{4}\sum_{q=n,p}\int d\boldsymbol{R}\;V_0^q\left[1-\frac{1}{2}\frac{\rho_0(\boldsymbol{R})}{\rho_c}\right]\tilde{\rho}^2(\boldsymbol{R}),\tag{52}$$

where $\tilde{\rho}(\boldsymbol{R})$ is the pairing density and $\rho_c=0.16$ fm^{-3}. The coefficients $C_t^{uu'}$ and V_0^q are the unknown parameters that we determine in the calibration process.

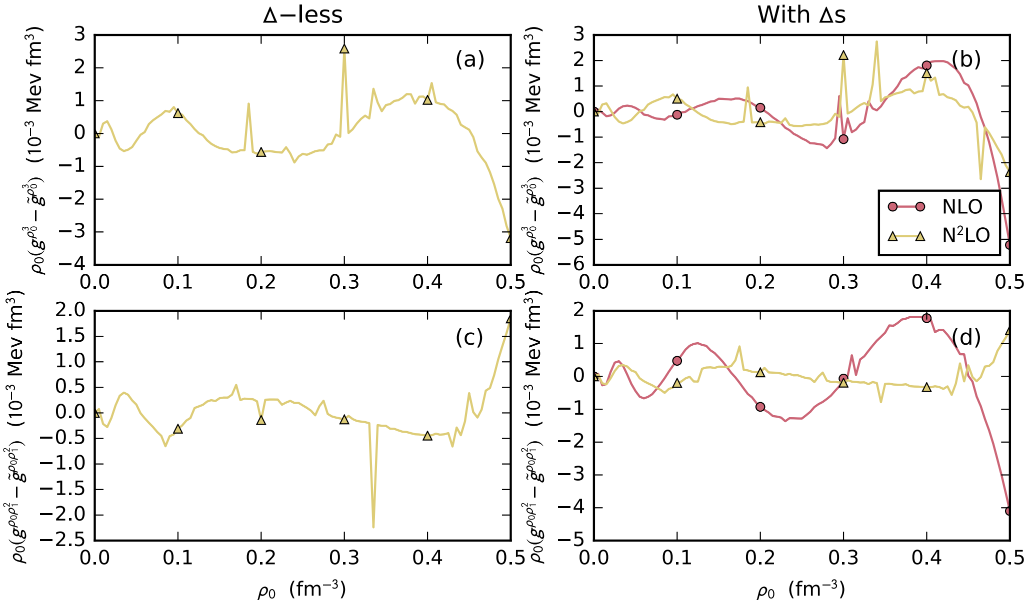

FIG. 3. Difference between the three-body density-dependent couplings $g^{\rho_0^3}$ and $g^{\rho_0\rho_1^2}$ and their corresponding interpolating functions $\tilde{g}^{\rho_0^3}$ and $\tilde{g}^{\rho_0\rho_1^2}$ given by Eq. (47). The irregularities in the curves show that the interpolation has an accuracy similar to the numerical multidimensional integral.

In practice, note that we are only fitting parameters in the NN exchange and pairing channel of the functional. The two-body Hartree term, Eq. (29), is computed "exactly" (that is, without any adjustment of parameters) and so is the three-body Fock term, Eq. (49).

For the optimization of the contact couplings, we follow the same prescription as for the UNEDF2 parametrization of the Skyrme functional [44]. Among the 14 parameters in Eqs. (50) and (52), $C_{t0}^{\rho\rho}$, $C_{tD}^{\rho\rho}$, $C_{t}^{\rho\tau}$, and γ are volume couplings and, therefore, can be directly related to infinite nuclear matter (INM) properties, which allows using tighter, physically motivated bounds; see Secs. IV.A-C and Appendix C in Ref. [23] for actual expressions relating INM properties with the coupling functions (51). In practice, we thus optimize the following INM parameters: ρ_c, E^{NM}, K^{NM}, M_s^{*-1}, $a_{\mathrm{sym}}^{\mathrm{NM}}$, and $L_{\mathrm{sym}}^{\mathrm{NM}}$. As with all UNEDF parametrizations of the Skyrme functional, we do not optimize the vector effective mass M_v^{*-1} but instead keep it fixed at its SLy4 value, $M_v^{*-1} = 1.249$. The remaining eight parameters are fitted directly with the same bounds as for UNEDF2.

Note that, in contrast to Skyrme EDFs, our DME EDFs contain a finite-range term that contributes to INM properties. The contribution of this finite-range term to the energy per particle for asymmetric nuclear matter reads [57]

$$e(\rho,\beta) = \frac{1}{2}\sum_{i=1}^{N}\Big\{A_0^i\rho + A_1^i\rho\beta^2 + B_{nn}^i\Big[\frac{1+\beta}{2}g\big(\mu_i k_F^n\big) + \frac{1-\beta}{2}g\big(\mu_i k_F^p\big)\Big] + B_{np}^i h\big(\mu_i k_F^n,\mu_i k_F^p\big)\Big\}, \tag{53}$$

where $\rho = \rho_n + \rho_p$ is the total density, $\beta = (\rho_n - \rho_p)/\rho$ the isospin asymmetry parameter, $k_F^n = k_F(1+\beta)^{1/3}$ and $k_F^p = k_F(1-\beta)^{1/3}$ are the Fermi momenta of the corresponding isospin symmetric system, the parameters A and B are

$$A_0^i = \frac{\pi^{3/2}\mu_i^3}{4}(4W_i + 2B_i - 2H_i - M_i), \tag{54}$$

$$A_1^i = \frac{\pi^{3/2}\mu_i^3}{4}(-2H_i - M_i), \tag{55}$$

$$B_{nn}^i = -\frac{1}{\sqrt{\pi}}(W_i + 2B_i - H_i - 2M_i), \tag{56}$$

$$B_{np}^i = \frac{1}{\sqrt{\pi}}(H_i + 2M_i), \tag{57}$$

and the functions $g(q)$ and $h(q_1,q_2)$ are the result of a double integration of the exchange matrix elements over the same Fermi surface for g, and two different surfaces for h, which result in

$$g(q) = \frac{2}{q^3} - \frac{3}{q} - \left(\frac{2}{q^3} - \frac{1}{q}\right)e^{-q^2} + \sqrt{\pi}\,\mathrm{erf}(q), \tag{58}$$

$$\begin{aligned} h(q_1,q_2) = {} & 2\frac{q_1^2 - q_1q_2 + q_2^2 - 2}{q_1^3 + q_2^3}e^{-\frac{(q_1+q_2)^2}{4}} \\ & - 2\frac{q_1^2 + q_1q_2 + q_2^2 - 2}{q_1^3 + q_2^3}e^{-\frac{(q_1-q_2)^2}{4}} \\ & - \sqrt{\pi}\frac{q_1^3 - q_2^3}{q_1^3 + q_2^3}\mathrm{erf}\left(\frac{q_1 - q_2}{2}\right) + \sqrt{\pi}\,\mathrm{erf}\left(\frac{q_1+q_2}{2}\right). \end{aligned} \tag{59}$$

The calculation of the INM properties simply requires performing a Taylor expansion around the saturation density ρ_c, which yields

$$e(\rho,\beta) = e(\rho) + S_2(\rho)\beta^2 + S_4(\rho)\beta^4 + \cdots, \tag{60}$$

TABLE I. Parameters of the various EDFs optimized in this work. The last line gives the value of the objective function at convergence of the optimization process. ρ_c is in fm^{-3}; E^{NM}, K^{NM}, $a_{\mathrm{sym}}^{\mathrm{NM}}$, and $L_{\mathrm{sym}}^{\mathrm{NM}}$ are in MeV; M_s^{*-1} is dimensionless; $C_t^{\rho\Delta\rho}$, $C_t^{\rho\nabla J}$, and C_t^{J} are in MeV fm^5; and V_0^n and V_0^p are in MeV fm^3.

	LO	NLO	N2LO	N2LO+3N	NLOΔ	NLOΔ+3N	N2LOΔ	N2LOΔ+3N
ρ_c	0.1544	0.1550	0.1584	0.1530	0.1586	0.1539	0.1556	0.1527
E^{NM}	– 15.8025	– 15.8000	– 15.8353	– 15.8133	– 15.8617	– 15.8135	– 15.8385	– 15.8417
K^{NM}	258.6536	254.9564	221.2413	250.3559	223.0304	250.0137	248.2058	259.2423
$a_{\mathrm{sym}}^{\mathrm{NM}}$	30.0578	30.5201	29.7554	29.2640	30.5042	29.6921	29.6983	30.4040
$L_{\mathrm{sym}}^{\mathrm{NM}}$	41.9577	42.9947	40.0000	40.2500	44.2077	40.0000	41.9412	40.0000
M_s^{*-1}	0.9763	0.9000	0.9048	0.9000	0.9000	0.9000	0.9000	0.9000
γ	0.5404	0.5238	0.3526	0.4931	0.3452	0.4711	0.4728	0.5301
$C_0^{\rho\Delta\rho}$	– 36.1843	– 52.6447	6.9892	– 29.1293	– 13.7870	– 33.2312	1.0440	– 35.3682
$C_1^{\rho\Delta\rho}$	– 70.2703	– 61.1454	– 65.9052	– 51.6414	– 68.9016	– 48.5797	– 69.1111	– 4.1573
V_0^n	– 194.7660	– 163.9659	– 164.2242	– 164.1451	– 163.3901	– 164.7202	– 163.1916	– 163.5773
V_0^p	– 227.1298	– 189.0806	– 191.1035	– 190.0664	– 188.7028	– 189.6970	– 189.0264	– 190.2702
$C_0^{\rho\nabla J}$	– 62.0154	– 62.1937	– 67.1676	– 72.8370	– 94.9189	– 75.8855	– 64.0646	– 69.6724
$C_1^{\rho\nabla J}$	– 81.2615	– 104.3616	– 71.2548	– 66.7901	– 40.3346	– 46.2612	– 37.6989	– 64.9767
C_0^{J}	– 101.8945	– 84.8842	– 100.4869	– 104.9008	– 18.7145	– 86.8496	– 112.1157	– 115.9108
C_1^{J}	34.4538	31.0748	– 41.5981	– 11.0683	39.6320	14.9317	– 10.3164	– 20.7663
$f(x)$	229.6620	164.1405	165.6655	167.6812	160.9050	165.2818	159.6821	162.6206

$$e(\rho) = \frac{E^{\mathrm{NM}}}{A} + \frac{P^{\mathrm{NM}}}{\rho_c}\delta\rho + \frac{K^{\mathrm{NM}}}{18\rho_c^2}(\delta\rho)^2 + \cdots , \quad (61)$$

$$S_2(\rho) = a_{\mathrm{sym}}^{\mathrm{NM}} + \frac{L_{\mathrm{sym}}^{\mathrm{NM}}}{3\rho_c} + \delta\rho + \cdots . \quad (62)$$

For detailed derivations of the finite-range contributions to the infinite nuclear matter properties see [57].

The new EDFs were optimized from LO to N2LO. The inclusion of a Δ excitation produces two additional versions of the functional at NLO and N2LO, denoted as NLOΔ and N2LOΔ. Finally the incorporation of 3N forces at the appropriate orders adds three more versions denoted as N2LO+3N, NLOΔ+3N and N2LOΔ+3N. Each of these eight EDFs has its own set of Gaussian functions to represent the finite-range contribution to the Hartree field, density-dependent couplings for the two- and three-body Fock fields, and calibrated two-body contact couplings to recover many-body correlations.

As already highlighted in Ref. [23], the parameter space of DME EDFs could be significantly different from that of traditional Skyrme EDFs. To avoid possible difficulties during the optimization process (which was initialized with the UNEDF2 parameter set), we took advantage of the built-in regulator (1): for large values of R_c, $f(r) \to 0$ and the finite-range contributions vanish. Therefore, the EDF reduces to a traditional Skyrme EDF. Starting from the UNEDF2 parameter set, we thus produced intermediate parametrizations of all the DME EDFs at $R_c = 2.0$ fm. As mentioned earlier, the final parametrizations were obtained with $R_c = 1.0$ fm.

It is important to note that the Δ-less and Δ-full versions of the chiral potential employ different sets of low-energy constants. In this work we derive the EDFs from the local potentials in coordinate space as presented in Ref. [25], for which the DME approximation was applied in Ref. [24]. The values for the LECs and other physical parameters used for the chiral potentials in this work are listed in Table I of Ref. [24].

The actual parameter sets of all eight DME EDFs are listed in Table I. The optimization was carried out with the POUNDERS optimization package from Argonne National Laboratory, with all HFB calculations performed with the HFBTHO solver with the exact same basis characteristics as in Ref. [44]. We notice that, for most DME EDFs, the scalar effective mass ends up at its bound. As expected, there are substantial variations among the different parametrizations, in particular when it comes to γ, $C_0^{\rho\Delta\rho}$, and C_1^{JJ}. Large fluctuations in the isovector channel are not surprising, since it is widely believed that the lack of constraints on these parameters comes from a lack of experimental data in very neutron-rich nuclei. The observed fluctuations in the power of the density dependence and the isoscalar surface terms are indicative of the strong non-linearity of the optimization process. With the exception of the EDF at LO, the value of the objective function is similar for all EDFs at around 164 ± 5, but we see in the next section that there are significant differences in predictive powers.

IV. VALIDATION AGAINST EXPERIMENTAL DATA

A. Infinite nuclear matter properties

We calculated the equation of state (EOS) with each of the new microscopically constrained EDFs. As mentioned in the

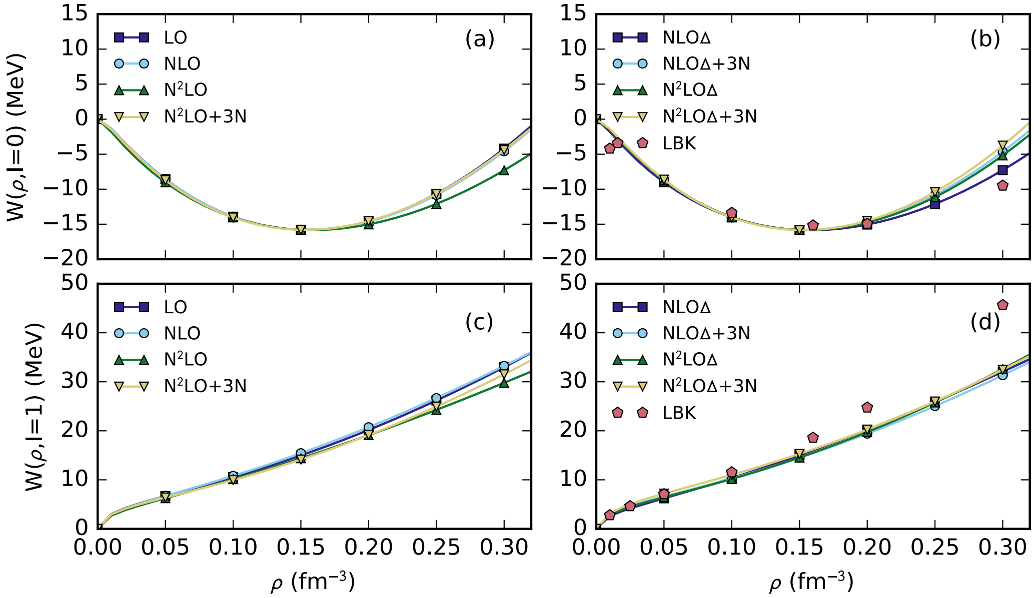

FIG. 4. Symmetric nuclear matter (top) and pure neutron matter (bottom) for the new DME functionals. For comparison we mark with red pentagons the calculation by Logoteta, Bombaci, and Kievsky (LBK) for a local chiral potential with delta isobar, labeled as N3LOΔ + N2LOΔ1 in Ref. [58].

previous section, the inclusion of density-dependent couplings and finite-range contributions in the density functional brings additional terms to the corresponding EOS. These terms were included following the derivations in Refs. [23,57]. In Fig. 4 we show the energy per nucleon E/A as a function of the density ρ for symmetric nuclear matter (SNM) and pure neutron matter (PNM).

Since the value of the saturation density and other INM properties at saturation were used to constrain the contact couplings for the EDFs, it is not surprising that all curves exhibit very similar behavior around the saturation point. The curves for the different EDFs start to deviate from one another at large values of ρ, especially for cases in which the $3N$ terms are not included even though the corresponding diagrams are present at such order. For the Δ-less implementation (left-hand panels), a convergence pattern can be seen when including the $3N$ terms; i.e., the difference between LO and NLO is larger than the difference between NLO and N2LO+$3N$. Unfortunately such a convergence pattern cannot be found in the Δ-full implementation.

As a reference point we include the recent calculation by Logoteta, Bombaci and Kievsky (LBK) for a local chiral potential with Δ isobar [58]. While a direct comparison cannot be done with our current results since the LBK calculations correspond to a Δ-full implementation of the two-body force at next-to-next-to-next-to-leading order (N3LO) and the $3N$ terms at N2LO, it still provides a useful reference. Also for comparison, the recent auxiliary field diffusion Monte Carlo simulations [59] using a chiral interaction at N2LO give an energy per nucleon for SNM between 12 and 16 MeV at saturation density depending on the value of the regulator. These simulations are in agreement with our calculations. Overall, our parametrization seems to yield a stiffer EOS than fully microscopic calculations.

B. Nuclear mass tables

For each of the EDFs listed in Table I, we computed the binding energies of all even-even nuclei from $Z = 8$ to $Z = 120$. The drip lines were identified by the requirement that the two-neutron separation energy change sign and become negative. For each even-even nucleus, we considered 11 different configurations characterized by their axial quadrupole deformation $\beta_2 = -0.25, \ldots, +0.25$ (by steps of 0.05). For each configuration, we used the small-deformation approximation of the quadrupole moment, $Q_2 \approx \beta_2\sqrt{5/\pi}(Z+N)^{5/3}/100$ (in barns), to impose a constraint on Q_2 for the HFB solution. The constraint was only active during the first 20 iterations of the self-consistent loop and was then automatically released. The binding energy retained for the even-even nucleus is then the lowest energy of these 11 configurations.

Binding energies of odd-even and odd-odd nuclei were not computed explicitly, as it would require performing numerous blocking calculations. There are at least two reasons why such an explicit calculation is not mandated here: (i) the main focus of this work is a global assessment of microscopically constrained EDFs, not the production of a mass model, and (ii) our optimization protocol, also used for the Skyrme UNEDF2 functional, does not put special emphasis on nuclear masses, which is one of five different types of observables. For these reasons, we rely instead on a popular approximation, where the energy of an odd-even nucleus $(Z-1,N)$ (with both Z and N even-even) is given by

$$\begin{aligned} E(Z-1,N) &= \tfrac{1}{2}[E(Z,N) + E(Z-2,N)] \\ &\quad + \tfrac{1}{2}[\Delta_p(Z,N) + \Delta_p(Z-2,N)], \qquad (63) \end{aligned}$$

with $\Delta_p(Z,N)$ the average proton pairing gap (obtained as $\Delta(Z,N) = \frac{1}{2}\mathrm{Tr}\Delta\rho_p$, where Δ is the pairing field of the HFB matrix). Similar formulas hold for even-odd nuclei. For odd-

TABLE II. Root mean square (rms) deviations between experimental and theoretical binding energies. Experimental values are taken from the 2016 Atomic Mass Evaluation [60,61]; see text for additional details.

EDF	rms	Number of nuclei
UNEDF2	1.98	620
LO	1.99	617
NLO	2.02	617
N2LO	1.57	616
N2LO+3N	1.58	613
NLOΔ	1.41	618
NLOΔ+3N	1.46	617
N2LOΔ	1.26	615
N2LOΔ+3N	1.72	617

TABLE III. Mean and standard deviations of the binding energy residuals for each of the eight EDFs considered in this work.

EDF	Mean	σ
UNEDF2	− 0.277	1.960
LO	− 0.288	1.971
NLO	− 1.144	1.659
N2LO	− 0.799	1.351
N2LO+3N	− 0.411	1.521
NLOΔ	− 0.480	1.327
NLOΔ+3N	− 0.461	1.386
N2LOΔ	− 0.343	1.209
N2LOΔ+3N	− 0.538	1.636

odd systems, we first compute

$$\Delta_p(Z,N-1) = \tfrac{1}{2}[\Delta_p(Z,N) + \Delta_p(Z,N-2)] \tag{64}$$

and, similarly, $\Delta_p(Z-2,N-1)$, and combine them to get

$$\begin{aligned} E(Z-1,N-1) = {} & \tfrac{1}{2}[E(Z,N-1) + E(Z-2,N-1)] \\ & + \tfrac{1}{2}[\Delta_p(Z,N-1) + \Delta_p(Z-2,N-1)]. \end{aligned} \tag{65}$$

All calculations were performed with the code HFBTHO in a deformed (stretched) basis of 20 shells with an axial deformation $\beta = \beta_2$.

Table II summarizes the characteristics of the mass tables for each EDF. It lists the rms deviation between theoretical and experimental nuclear binding energies as well as the number of experimental measurements. Experimental atomic masses are taken from the 2016 Atomic Mass Evaluation [60,61]. Nuclear binding energies are obtained after taking into account the binding energy of the electrons. Following Ref. [61], we adopt the following empirical formula:

$$B_e(Z) = 1.44381 \times 10^{-5} Z^{2.39} + 1.55468 \times 10^{-12} Z^{5.35} \tag{66}$$

with the energy given in MeV. We only included true experimental measurements and did not take into account evaluated masses. Further details on how nuclear binding energies are extracted from the mass evaluation can be found in Ref. [42].

Perhaps the most surprising (and promising) result is the relatively large variation of the results, with a rms ranging from 1.26 MeV for N2LOΔ to 2.02 MeV for NLO—a 60% difference in predictive power. It is also very encouraging to note that the EDFs seem to perform better and better overall as we go from LO to NLO to N2LO and add Δ excitations when only NN contributions are included. In fact, the quality of the N2LO+Δ EDF is rather spectacular. Without any "beyond-mean-field" corrections such as the rotational or vibrational corrections, Wigner energy, etc., this EDF does markedly better than UNEDF2. Remember that (i) the determination of the EDF parameters was made with the exact same protocol and optimizer and (ii) all mass tables were computed with the exact same code, basis characteristics, and overall algorithms to identify drip lines. Therefore, the origin of all differences listed in Table II can be attributed to the form of the EDF only.

However, the impact of the 3N contributions is puzzling. At N2LO and NLOΔ the rms is unchanged or even slightly worse when the 3N is added to the functional. At N2LO+Δ there is a significant degradation. At present we do not understand these trends.

A visual representation of the difference between theory and experiment highlights a few additional interesting features of these EDFs. For light nuclei, Fig. 5 shows that the LO and NLO EDFs behave like the UNEDF2 (and older UNEDF1) EDF: discrepancies with experimental masses are larger, which was explained in Refs. [43,44] as resulting from neglecting the center-of-mass correction in the EDF—a choice that we also made for all the DME EDFs. Surprisingly, this feature is much attenuated for EDFs based on higher-order chiral potentials.

We also notice that both EDFs including the effect of three-body force and, to a lesser extent, that of the Δ excitations have more pronounced spikes near closed-shell nuclei, as shown by comparing, e.g., the mass tables for N2LO and N2LO+3N, or N2LOΔ and N2LOΔ+3N. Overall, we also notice that the effect of the three-body force seems to be the largest near closed shells, in particular near ^{208}Pb.

Table III completes the picture by showing the mean value and standard deviations computed from the residuals of nuclear binding energies. Compared with UNEDF2 and LO (which is not much different from UNEDF2 by construction), DME functionals have a larger systematic bias—which also tends to decrease as we go to higher order in the χ_{EFT} expansion. Conversely, the standard deviation for the DME functionals is much smaller than for Skyrme, and the trend is also towards smaller standard deviations. Recall that for a random variable with mean μ and standard deviation σ, we have $\mathrm{rms}^2 = \sigma^2 + \mu^2$.

Another indicator of the global quality of an EDF is the proton radius. We show in Fig. 6 the residuals for proton radii for the 339 nuclei listed in Ref. [62] in the two particular cases of the UNEDF2 and the NLOΔ+3N functionals. We extracted experimental proton radii from the table of Ref. [62] by using the formula

$$r_{\mathrm{ch}}^2 = \langle r_p^2 \rangle + r_p^2 + \frac{N}{Z} r_n^2 \tag{67}$$

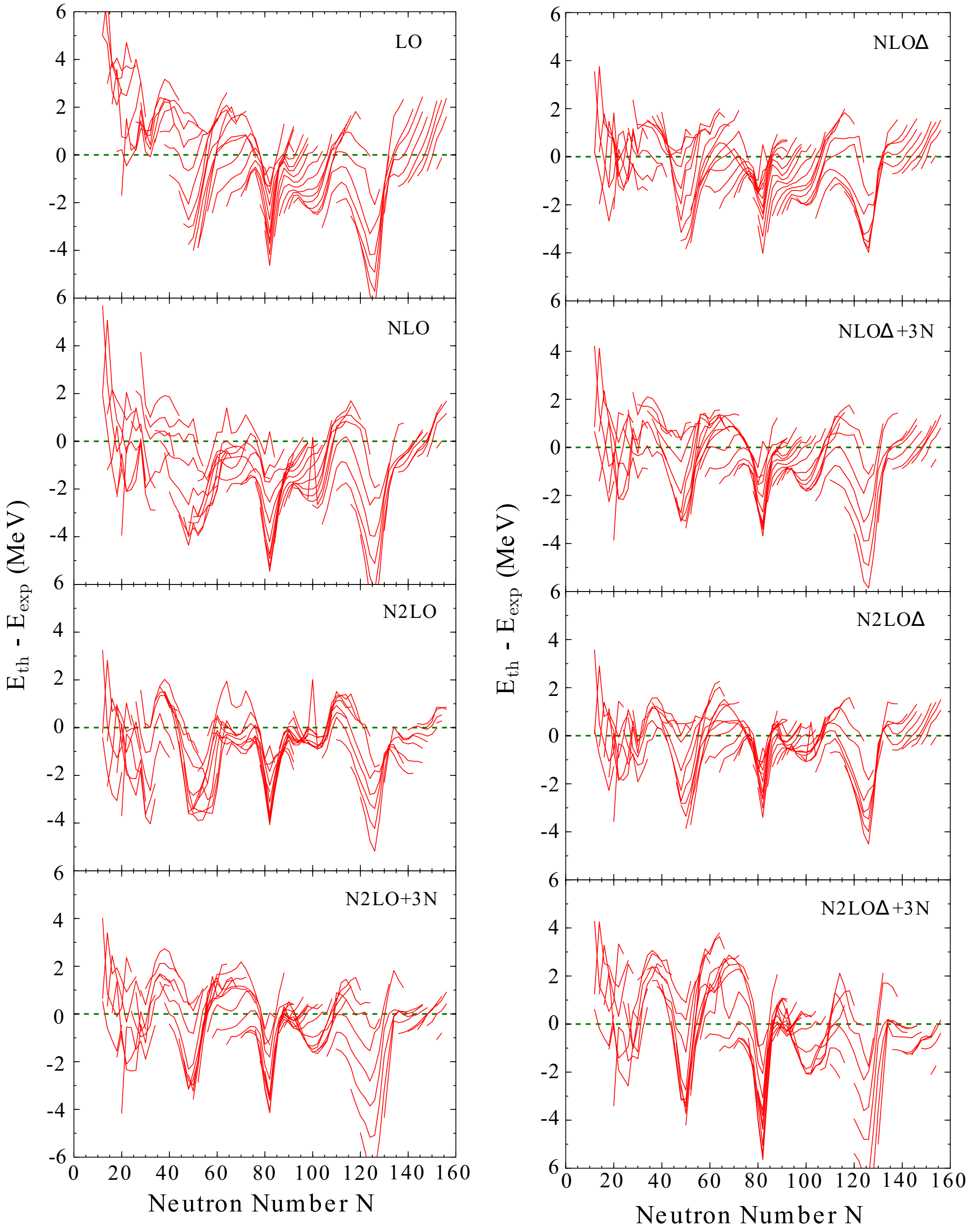

FIG. 5. Deviations between theoretical and experimental binding energies for even-even nuclei. Experimental binding energies are extracted from the 2016 mass evaluation [60,61] and only actual measured values are used. Left, EDFs without Δ excitations; right, EDFs with Δ excitations.

with r_{ch}^2 the charge radius of the nucleus, $\langle r_p^2 \rangle$ the expectation value of the proton radius on the HFB solution, and $r_n^2 = -0.1161\ \mathrm{fm}^2$ and $r_p^2 = 0.769\ \mathrm{fm}^2$ the charge mean square radii of the free neutron and proton, respectively. Table IV lists the rms, mean value, and standard deviation of the residuals for all eight functionals listed in Table I. Overall, the prediction of proton radii is on par with competing functionals (see, e.g., Refs. [14,63]), although it is slightly worse than for the Skyrme UNEDF2. We also observe a similar effect as for masses: DME functionals have a larger systematic bias than the pure Skyrme UNEDF2. However, this bias is very small (<0.01 fm) and may not be very significant.

C. Shell structure

We turn to the s.p. shell structure of closed-shell nuclei. As a reminder, we extract s.p. energies of the nucleus (Z,N) by performing blocking calculations [64] at the equal filling approximation [65] in the neighboring odd nuclei, e.g., $(Z,N \pm 1)$ for neutron s.p. states; see, e.g., Refs. [66–71] for studies

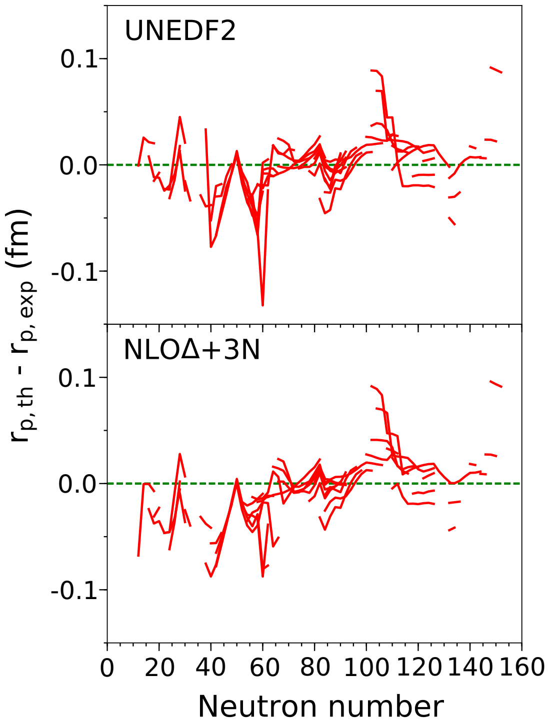

FIG. 6. Proton radii residuals for the UNEDF2 (top) and NLOΔ+3N (bottom) functionals. Experimental data are taken from Ref. [62].

of the blocking prescription on the ground-state properties of odd nuclei. Specifically, we define

$$E_{\text{s.p.}}^{(\text{particle})} = E_{\text{bl}}(A+1) - E(A), \tag{68a}$$

$$E_{\text{s.p.}}^{(\text{hole})} = E(A) - E_{\text{bl}}(A-1), \tag{68b}$$

where A is the particle number of the reference, doubly magic, nucleus of interest and E_{bl} is the energy of the blocked configuration in the neighboring odd nucleus. The labels "hole" and "particle" refer to whether the corresponding s.p. levels would be, respectively, fully occupied or empty in the corresponding HF calculation of the doubly magic nucleus.

TABLE IV. The rms, mean, and standard deviations, in femtometers, for the proton radius residuals for each of the eight EDFs considered in this work.

EDF	rms	Mean	σ
UNEDF2	0.027449	+0.000373	0.027487
LO	0.028710	− 0.000465	0.028749
NLO	0.033489	− 0.003573	0.033347
N2LO	0.033558	− 0.002725	0.033496
N2LO+3N	0.035225	+0.001547	0.035243
NLOΔ	0.028432	− 0.006602	0.027695
NLOΔ+3N	0.031102	− 0.003854	0.030908
N2LOΔ	0.029878	− 0.004295	0.029611
N2LOΔ+3N	0.032645	− 0.000004	0.032694

This method presents two advantages. First, it ensures the consistency of the calculations for all observables. Whether we consider masses, s.p. energies, or fission barriers, we always perform computations in the same HFB framework with the Lipkin-Nogami correction. Second, we automatically include the small shape polarization induced by the blocking calculation—even though this polarization is restricted here to axial shapes owing to the built-in symmetries of HFBTHO [70,71].

We recall that in HFBTHO, blocking configurations can only be specified by the Nilsson quantum numbers $[Nn_z\Lambda]\Omega$ of the requested s.p. state (see Ref. [72] for details). Since these quantum numbers are only valid approximately (Ω corresponds to a conserved symmetry of the mean field, but not the others; see Ref. [73] for a discussion), the convergence of the blocking calculations can sometimes fail. In particular, we found that for low-j orbitals, we had to introduce tiny constraints either on the expectation value of $\hat{Q}_2$ or $\hat{Q}_4$ in order to converge the blocking calculations. Since the effective s.p. energy is defined as an energy difference, the numerical error introduced is very small—less than 50 keV overall. Note that similar difficulties were experienced with the UNEDF family of EDFs presented in Refs. [42–44].

Figure 7 shows the example of neutron s.p. states in ^{208}Pb for the various EDFs listed in Table I. Contrary to binding energies, we do not observe a very clear improvement or degradation of the shell structure as a function of the EDF used. The s.p. spectrum in other closed-shell nuclei yields similar conclusions. This could be attributed to the fact that the optimization protocol is the same for all EDFs and explicitly includes a constraint on a few spin-orbit splittings. In addition, work with either Skyrme EDF or covariant DFT suggests that correlations such as particle-vibration couplings play a major role in improving the shell structure in closed-shell nuclei. It is unlikely that the DME functionals we consider have this type of correlations built in.

D. Deformation properties

As mentioned in the Introduction, one of the primary applications of DFT is the study of nuclear structure and excited states for deformed nuclei, including rotational and vibrational spectra and fission. Although the shell structure of closed-shell nuclei discussed in the previous section and the large-scale mass tables shown in Fig. 5 are indicative of an EDF with a good overall predictive power, it is important to also test the behavior of the EDF at large deformations. For this reason, the UNEDF2 optimization protocol includes the excitation energy of a few fission isomers in actinides. As discussed in Refs. [43,74], this provides constraints on both the shell structure—inasmuch as deformation properties are partly driven by the particular ordering and level density of s.p. j shells in spherical nuclei—and on surface properties of the EDF, which are related in particular to $a_{\text{sym}}^{\text{NM}}$.

We report in Table V the excitation energy of the fission isomer and height of the first and second barriers extracted from calculations of the potential energy curve in ^{240}Pu. Across all eight DME EDFs, the rms deviation for the excitation energy of the fission isomer is 0.29 MeV, which is comparable to the

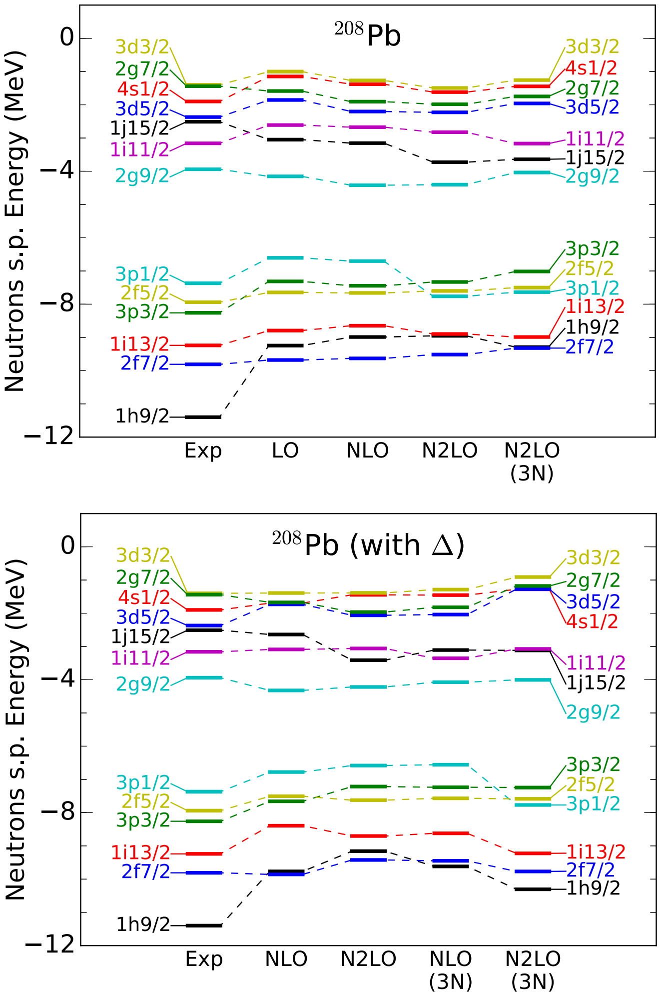

FIG. 7. Neutron s.p. levels in ^{208}Pb extracted from blocking calculations. In the top panel, EDFs derived from NN and $3N$ forces without Δ excitations are included; in the bottom panel, EDFs derived from NN+$3N$ forces with Δ excitations are shown.

TABLE V. Excitation energy of the fission isomer and height of the first and second fission barriers in ^{240}Pu for each of the eight DME EDFs, compared with empirical values in MeV. The column marked E_A (est.) includes an approximate 2.5 MeV correction on the height of the first barrier to account for the fact that calculations were done in axial symmetry.

	$E_{\rm FI}$	E_A	E_A (est.)	E_B
LO	2.625	9.479	6.979	6.468
NLO	2.893	9.122	6.622	5.634
N2LO	2.784	9.472	6.972	5.998
N2LO+3N	2.481	8.992	6.492	6.955
NLOΔ	2.395	10.064	7.564	6.235
NLOΔ+3N	2.387	8.901	6.401	6.652
N2LOΔ	2.691	9.967	7.467	7.214
N2LOΔ+3N	2.350	12.162	9.662	7.530
Expt.	2.800		6.050	5.150

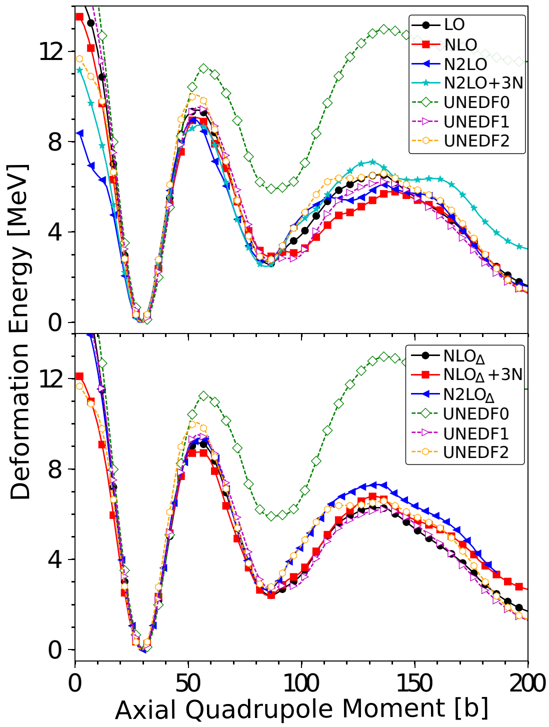

FIG. 8. Deformation potential energy surface in ^{240}Pu as a function of the axial quadrupole moment. Top: Energy functionals at LO, NLO, and N2LO, with and without $3N$ forces (when applicable). Bottom: Same for EDF based on potentials including the Δ contribution. For comparison, each panel also shows the results for the UNEDF0, UNEDF1, and UNEDF2 functionals of Refs. [42–44].

predictive power of the UNEDF Skyrme functionals across all actinides (see Ref. [44]). However, fission barriers tend to be too high—even when taking into account the extra ≈2.5 MeV caused by the lack of triaxiality in calculations of the first barrier [the column marked E_A (est.) in the table] For example, the rms deviation for the second barrier is 1.55 MeV, compared with 1.39 MeV for UNEDF2 and 0.69 MeV for UNEDF1 (across all actinides). We show in the two panels of Fig. 8 the potential energy curve of ^{240}Pu as a function of the axial quadrupole moment for all eight EDFs considered here and listed in Table I, together with that of the UNEDF0, UNEDF1, and UNEDF2 functionals for comparison.

V. CONCLUSIONS

In this work, we have calibrated and validated a set of energy density functionals derived from local chiral potentials through the DME. We have provided the parametrization of these EDFs at LO, NLO, N2LO, N2LO+3N, NLOΔ, NLOΔ+3N, N2LOΔ, and N2LOΔ+3N for a value of $R_c = 1.0$ fm and $n = 6$ in the regulator cutoff. The optimization was performed with the UNEDF2 protocol, and results were validated on the EOS of infinite nuclear matter and pure neutron matter, nuclear mass tables, the shell structure of doubly-closed-shell nuclei, and the deformation energy of ^{240}Pu.

The overall predictive power of these EDFs is better than the Skyrme EDFs obtained with the same optimization protocol. The relatively large variations among the eight considered parametrizations is very encouraging as it suggests that even without "beyond-mean-field effects" such as zero-point correlation energies, particle-vibration couplings, etc., observables such as binding energies are sensitive to the details of the EDF. It is remarkable that, on average, the quality of the prediction increases noticeably as one goes higher in the chiral expansion when only NN contributions are included. However, the addition of $3N$ contributions leaves observables essentially unchanged or, for the case of the N2LOΔ+$3N$ EDF, the predictions of binding energies and even the s.p. structure degrade relative to other EDFs. We do not have an explanation at present for the $3N$ behavior but are investigating several avenues.

One should also keep in mind that, from a statistical perspective, calibrating functionals at the single-reference level implies that the model has "defects," i.e., it is not designed to accurately reproduce specific observables (see discussion in Sec. III). In practice, trying to fit both binding energies in closed-shell nuclei like ^{208}Pb and well-deformed nuclei in the rare-earth region could lead to overfitting issues.

In this work, we have left out the estimate of uncertainties—only quantifying numerical errors induced by approximating Yukawa form factors by a sum of Gaussian functions and by interpolating coupling functions. In particular, it could be worth studying in more detail the exchange contribution to the energy by (i) calibrating a Hartree-only functional where the exchange contribution of the long-range chiral potential would be dropped entirely, and, conversely, (ii) calibrating a functional where the Fock contribution from the chiral potential would be computed exactly by expanding it onto a sum of Gaussians, like the Hartree term. If we restrict ourselves to NN potentials only, the computational effort is not significantly larger.

Since the DME EDFs originate from NN and $3N$ potentials from chiral perturbation theory and their coupling constants have been determined with the exact same optimization protocol, these EDFs lend themselves particularly well to studies of systematic uncertainties. Together with the well-established machinery to quantify statistical uncertainties with either covariance or Bayesian methods, such studies could shed more light on the true predictive power of these EDFs. Since the DME functionals seem to encode some effects traditionally associated with beyond-mean-field physics, it would also be natural to explore fits at the MR-EDF level. Doing it exactly through, e.g., configuration mixing with the generator coordinate method (GCM) or restoration of broken symmetries could be very challenging, because of the formal difficulties of combining non-integer powers of the density in the functional with these techniques [51,75–77]. Approximate methods such as the Lipkin method to emulate symmetry restoration [54,78] or the Gaussian overlap approximation to the GCM [79–81] could be interesting compromises.

ACKNOWLEDGMENTS

Support for this work was partly provided through the Scientific Discovery through Advanced Computing (SciDAC) program funded by the US Department of Energy, Office of Science, Advanced Scientific Computing Research and Nuclear Physics. It was partly performed under the auspices of the US Department of Energy by the Lawrence Livermore National Laboratory (LLNL) under Contract No. DE-AC52-07NA27344. This work was supported by the US Department of Energy under Grant No. DE-FG02-93ER-40756, the National Science Foundation under Grant No. PHY–1614460, and the NUCLEI SciDAC Collaboration under DOE Grants No. DE-SC0008533 and No. RC107839-OSU. Computing support for this work came from the LLNL Institutional Computing Grand Challenge program.

[1] E. Epelbaum and U.-G. Meißner, Annu. Rev. Nucl. Part. Sci. **62**, 159 (2012).
[2] R. Machleidt and F. Sammarruca, Phys. Scr. **91**, 083007 (2016).
[3] B. R. Barrett, P. Navrátil, and J. P. Vary, Prog. Part. Nucl. Phys. **69**, 131 (2013).
[4] J. Carlson, S. Gandolfi, F. Pederiva, S. C. Pieper, R. Schiavilla, K. E. Schmidt, and R. B. Wiringa, Rev. Mod. Phys. **87**, 1067 (2015).
[5] G. Hagen, T. Papenbrock, M. Hjorth-Jensen, and D. J. Dean, Rep. Prog. Phys. **77**, 096302 (2014).
[6] H. Hergert, S. K. Bogner, T. D. Morris, A. Schwenk, and K. Tsukiyama, Phys. Rep. **621**, 165 (2016).
[7] M. Bender, P.-H. Heenen, and P.-G. Reinhard, Rev. Mod. Phys. **75**, 121 (2003).
[8] J. Stone and P.-G. Reinhard, Prog. Part. Nucl. Phys. **58**, 587 (2007).
[9] P. Becker, D. Davesne, J. Meyer, J. Navarro, and A. Pastore, Phys. Rev. C **96**, 044330 (2017).
[10] F. Raimondi, B. G. Carlsson, J. Dobaczewski, and J. Toivanen, Phys. Rev. C **84**, 064303 (2011).
[11] B. G. Carlsson, J. Dobaczewski, and M. Kortelainen, Phys. Rev. C **78**, 044326 (2008).
[12] F. Raimondi, K. Bennaceur, and J. Dobaczewski, J. Phys. G: Nucl. Part. Phys. **41**, 055112 (2014).
[13] M. Baldo, L. M. Robledo, P. Schuck, and X. Viñas, Phys. Rev. C **95**, 014318 (2017).
[14] M. Baldo, L. M. Robledo, P. Schuck, and X. Viñas, Phys. Rev. C **87**, 064305 (2013).
[15] M. Baldo, P. Schuck, and X. Viñas, Phys. Lett. B **663**, 390 (2008).
[16] A. Bulgac, M. M. Forbes, S. Jin, R. Navarro Perez, and N. Schunck, Phys. Rev. C **97**, 044313 (2018).
[17] J. W. Negele and D. Vautherin, Phys. Rev. C **5**, 1472 (1972).
[18] J. W. Negele and D. Vautherin, Phys. Rev. C **11**, 1031 (1975).
[19] B. Gebremariam, S. K. Bogner, and T. Duguet, Nucl. Phys. A **851**, 17 (2011).

[20] B. Gebremariam, T. Duguet, and S. K. Bogner, Phys. Rev. C **82**, 014305 (2010).

[21] J. Dobaczewski, B. G. Carlsson, and M. Kortelainen, J. Phys. G: Nucl. Part. Phys. **37**, 075106 (2010).

[22] B. Carlsson, J. Dobaczewski, J. Toivanen, and P. Veselý, Comput. Phys. Commun. **181**, 1641 (2010).

[23] M. Stoitsov, M. Kortelainen, S. K. Bogner, T. Duguet, R. J. Furnstahl, B. Gebremariam, and N. Schunck, Phys. Rev. C **82**, 054307 (2010).

[24] A. Dyhdalo, S. K. Bogner, and R. J. Furnstahl, Phys. Rev. C **95**, 054314 (2017).

[25] M. Piarulli, L. Girlanda, R. Schiavilla, R. N. Pérez, J. E. Amaro, and E. R. Arriola, Phys. Rev. C **91**, 024003 (2015).

[26] M. Piarulli, L. Girlanda, R. Schiavilla, A. Kievsky, A. Lovato, L. E. Marcucci, S. C. Pieper, M. Viviani, and R. B. Wiringa, Phys. Rev. C **94**, 054007 (2016).

[27] E. Epelbaum, H. Krebs, and U. G. Meißner, Phys. Rev. Lett. **115**, 122301 (2015).

[28] A. Ekström, G. R. Jansen, K. A. Wendt, G. Hagen, T. Papenbrock, B. D. Carlsson, C. Forssén, M. Hjorth-Jensen, P. Navrátil, and W. Nazarewicz, Phys. Rev. C **91**, 051301(R) (2015).

[29] B. D. Carlsson, A. Ekström, C. Forssén, D. F. Strömberg, G. R. Jansen, O. Lilja, M. Lindby, B. A. Mattsson, and K. A. Wendt, Phys. Rev. X **6**, 011019 (2016).

[30] P. Reinert, H. Krebs, and E. Epelbaum, arXiv:1711.08821.

[31] B. Long and V. Lensky, Phys. Rev. C **83**, 045206 (2011).

[32] M. C. M. Rentmeester, R. G. E. Timmermans, J. L. Friar, and J. J. de Swart, Phys. Rev. Lett. **82**, 4992 (1999).

[33] P. Buettiker and U.-G. Meissner, Nucl. Phys. A **668**, 97 (2000).

[34] M. C. M. Rentmeester, R. G. E. Timmermans, and J. J. de Swart, Phys. Rev. C **67**, 044001 (2003).

[35] D. R. Entem and R. Machleidt, Phys. Rev. C **68**, 041001 (2003).

[36] M. Pavon Valderrama and E. Ruiz Arriola, Phys. Rev. C **74**, 054001 (2006).

[37] H. Krebs, E. Epelbaum, and U.-G. Meissner, Eur. Phys. J. A **32**, 127 (2007).

[38] A. Ekström, G. Baardsen, C. Forssén, G. Hagen, M. Hjorth-Jensen, G. R. Jansen, R. Machleidt, W. Nazarewicz, T. Papenbrock, J. Sarich, and S. M. Wild, Phys. Rev. Lett. **110**, 192502 (2013).

[39] R. Navarro Pérez, J. E. Amaro, and E. Ruiz Arriola, Phys. Rev. C **89**, 024004 (2014).

[40] M. P. Valderrama and E. R. Arriola, Phys. Rev. C **79**, 044001 (2009).

[41] M. Pavon Valderrama and E. Ruiz Arriola, Phys. Rev. C **83**, 044002 (2011).

[42] M. Kortelainen, T. Lesinski, J. Moré, W. Nazarewicz, J. Sarich, N. Schunck, M. V. Stoitsov, and S. Wild, Phys. Rev. C **82**, 024313 (2010).

[43] M. Kortelainen, J. McDonnell, W. Nazarewicz, P.-G. Reinhard, J. Sarich, N. Schunck, M. V. Stoitsov, and S. M. Wild, Phys. Rev. C **85**, 024304 (2012).

[44] M. Kortelainen, J. McDonnell, W. Nazarewicz, E. Olsen, P.-G. Reinhard, J. Sarich, N. Schunck, S. M. Wild, D. Davesne, J. Erler, and A. Pastore, Phys. Rev. C **89**, 054314 (2014).

[45] A. Bulgac, S. Jin, P. Magierski, K. Roche, N. Schunck and I. Stetcu, EPJ Web Conf. **163**, 00007 (2017).

[46] W. Satuła and W. Nazarewicz, Phys. Scr. **91**, 023013 (2016).

[47] M. Bender, G. F. Bertsch, and P.-H. Heenen, Phys. Rev. C **73**, 034322 (2006).

[48] P. Klüpfel, P.-G. Reinhard, T. J. Bürvenich, and J. A. Maruhn, Phys. Rev. C **79**, 034310 (2009).

[49] G. Colò, H. Sagawa, and P. F. Bortignon, Phys. Rev. C **82**, 064307 (2010).

[50] T. Lesinski, Ph.D. thesis, Université Claude Bernard–Lyon I, Lyon, 2008 (unpublished).

[51] T. Duguet, M. Bender, K. Bennaceur, D. Lacroix, and T. Lesinski, Phys. Rev. C **79**, 044320 (2009).

[52] K. Hebeler, T. Duguet, T. Lesinski, and A. Schwenk, Phys. Rev. C **80**, 044321 (2009).

[53] D. W. L. Sprung, M. Vallieres, X. Campi, and C.-M. Ko, Nucl. Phys. A **253**, 1 (1975).

[54] J. Dobaczewski, W. Satuła, B. Carlsson, J. Engel, P. Olbratowski, P. Powałowski, M. Sadziak, J. Sarich, N. Schunck, A. Staszczak, M. Stoitsov, M. Zalewski, and H. Zduńczuk, Comput. Phys. Commun. **180**, 2361 (2009).

[55] W. Younes, Comput. Phys. Commun. **180**, 1013 (2009).

[56] R. N. Perez, N. Schunck, R. D. Lasseri, C. Zhang, and J. Sarich, Comput. Phys. Commun. **220**, 363 (2017).

[57] R. Sellahewa and A. Rios, Phys. Rev. C **90**, 054327 (2014).

[58] D. Logoteta, I. Bombaci, and A. Kievsky, Phys. Rev. C **94**, 064001 (2016).

[59] I. Tews, S. Gandolfi, A. Gezerlis, and A. Schwenk, Phys. Rev. C **93**, 024305 (2016).

[60] W. Huang, G. Audi, M. Wang, F. Kondev, S. Naimi, and X. Xu, Chin. Phys. C **41**, 030002 (2017).

[61] M. Wang, G. Audi, F. Kondev, W. Huang, S. Naimi, and X. Xu, Chin. Phys. C **41**, 030003 (2017).

[62] I. Angeli and K. Marinova, Atom. Data Nucl. Data Tables **99**, 69 (2013).

[63] S. Goriely, N. Chamel, and J. M. Pearson, Phys. Rev. C **88**, 061302 (2013).

[64] P. Ring and P. Schuck, *The Nuclear Many-Body Problem* (Springer-Verlag, Berlin, 2000).

[65] S. Perez-Martin and L. M. Robledo, Phys. Rev. C **78**, 014304 (2008).

[66] K. Rutz, M. Bender, P.-G. Reinhard, J. A. Maruhn, and W. Greiner, Nucl. Phys. A **634**, 67 (1998).

[67] K. Rutz, M. Bender, P.-G. Reinhard, and J. A. Maruhn, Phys. Lett. B **468**, 1 (1999).

[68] T. Duguet, P. Bonche, P.-H. Heenen, and J. Meyer, Phys. Rev. C **65**, 014310 (2001).

[69] T. Duguet, P. Bonche, P.-H. Heenen, and J. Meyer, Phys. Rev. C **65**, 014311 (2001).

[70] N. Schunck, J. Dobaczewski, J. McDonnell, J. Moré, W. Nazarewicz, J. Sarich, and M. V. Stoitsov, Phys. Rev. C **81**, 024316 (2010).

[71] D. Tarpanov, J. Toivanen, J. Dobaczewski, and B. G. Carlsson, Phys. Rev. C **89**, 014307 (2014).

[72] M. Stoitsov, N. Schunck, M. Kortelainen, N. Michel, H. Nam, E. Olsen, J. Sarich, and S. Wild, Comput. Phys. Commun. **184**, 1592 (2013).

[73] A. Bohr and B. Mottelson, *Nuclear Structure*, Vol. II (Benjamin, New York, 1975).

[74] N. Nikolov, N. Schunck, W. Nazarewicz, M. Bender, and J. Pei, Phys. Rev. C **83**, 034305 (2011).

[75] M. V. Stoitsov, J. Dobaczewski, R. Kirchner, W. Nazarewicz, and J. Terasaki, Phys. Rev. C **76**, 014308 (2007).

[76] D. Lacroix, T. Duguet, and M. Bender, Phys. Rev. C **79**, 044318 (2009).

[77] M. Bender, T. Duguet, and D. Lacroix, Phys. Rev. C **79**, 044319 (2009).

[78] X. B. Wang, J. Dobaczewski, M. Kortelainen, L. F. Yu, and M. V. Stoitsov, Phys. Rev. C **90**, 014312 (2014).

[79] S. G. Rohoziński, J. Phys. G: Nucl. Part. Phys. **42**, 025109 (2015).

[80] S. G. Rohoziński, J. Phys. G: Nucl. Part. Phys. **39**, 095104 (2012).

[81] J.-P. Delaroche, M. Girod, J. Libert, H. Goutte, S. Hilaire, S. Péru, N. Pillet, and G. F. Bertsch, Phys. Rev. C **81**, 014303 (2010).